Wang, L., Hainzl, S., Zöller, G., Holschneider, M. (2012): Stress- and aftershock-constrained joint inversions for coseismic and postseismic slip applied to the 2004 M6.0 Parkfield earthquake. - Journal of Geophysical Research, 117, B07406

DOI: 10.1029/2011JB009017

Stress- and aftershock-constrained joint inversions for coseismic and postseismic slip applied to the 2004 M6.0 Parkfield earthquake

Lifeng Wang,[1,2] Sebastian Hainzl,[3] Gert Zöller,[1] and Matthias Holschneider[1]

Received 12 November 2011; revised 30 May 2012; accepted 31 May 2012; published 19 July 2012.

[1] Both aftershocks and geodetically measured postseismic displacements are important markers of the stress relaxation process following large earthquakes. Postseismic displacements can be related to creep-like relaxation in the vicinity of the coseismic rupture by means of inversion methods. However, the results of slip inversions are typically non-unique and subject to large uncertainties. Therefore, we explore the possibility to improve inversions by mechanical constraints. In particular, we take into account the physical understanding that postseismic deformation is stress-driven, and occurs in the coseismically stressed zone. We do joint inversions for coseismic and postseismic slip in a Bayesian framework in the case of the 2004 M6.0 Parkfield earthquake. We perform a number of inversions with different constraints, and calculate their statistical significance. According to information criteria, the best result is preferably related to a physically reasonable model constrained by the stress-condition (namely postseismic creep is driven by coseismic stress) and the condition that coseismic slip and large aftershocks are disjunct. This model explains 97% of the coseismic displacements and 91% of the postseismic displacements during day 1–5 following the Parkfield event, respectively. It indicates that the major postseismic deformation can be generally explained by a stress relaxation process for the Parkfield case. This result also indicates that the data to constrain the coseismic slip model could be enriched postseismically. For the 2004 Parkfield event, we additionally observe asymmetric relaxation process at the two sides of the fault, which can be explained by material contrast ratio across the fault of $\sim$1.15 in seismic velocity.

Citation: Wang, L., S. Hainzl, G. Zöller, and M. Holschneider (2012), Stress- and aftershock-constrained joint inversions for coseismic and postseismic slip applied to the 2004 M6.0 Parkfield earthquake, *J. Geophys. Res.*, *117*, B07406, doi:10.1029/2011JB009017.

1. Introduction

[2] The seismic cycle in general includes several phases, interseismic, nucleation, coseismic and postseismic phase. In the interseismic phase, strain gradually builds up around the locked fault in tens to thousands of years, while it is coseismically released in seconds. The nucleation phase is characterized by low seismic moment release rate on time-scales up to months and is usually hard to be captured by contemporary instruments [e.g., *Ellsworth and Beroza*, 1995; *Dieterich and Kilgore*, 1996]. In the postseismic interval, stress relaxation lasts months to years, indicated by abundance of aftershock seismicity and evident aseismic deformations in or around the fault zone. It has been indicated that the postseismic activities usually release a large amount of strain which can be comparable to or even higher than the main shocks themselves [*Pritchard et al.*, 2006, and reference therein]. Therefore, the postseismic processes play an important role in the whole seismic cycle, and their relations to the main rupture are of particular interest for understanding the fault mechanics. Benefiting from the development of geodetic observatory, e.g., Global Positioning System (GPS) and Interferometric Synthetic Aperture Radar (InSAR) in the last two decades, the postseismic observations have been significantly improved and become valuable information for understanding both the rheology of the fault zone and regional stress evolution [e.g., *Savage et al.*, 1994; *Bürgmann et al.*, 1997; *Khazaradze and Klotz*, 2003; *Pollitz et al.*, 2008].

[3] Some mechanisms have been proposed to connect aftershocks, postseismic deformation, and coseismic rupture. *Scholz* [1968] presented that stress corrosion in response to coseismic stress perturbation produces microfracture or fault creep around the main rupture. Some of these microfractures would trigger larger fractures that produce big aftershocks. *Dieterich* [1994] explained aftershocks as the result of rate-and-state dependent frictional nucleation in response to the coseismic static stress changes related to main shock. Within

[1]Institute of Mathematics, University of Potsdam, Potsdam, Germany.
[2]China Earthquake Networks Center, Beijing, China.
[3]GFZ German Research Centre for Geosciences, Potsdam, Germany.

Corresponding author: L. Wang, Institute of Mathematics, University of Potsdam, Karl-Liebknecht-Str. 24, Potsdam D-14476, Germany. (wanglf@gfz-potsdam.de)

0148-0227/12/2011JB009017

the same framework, *Marone et al.* [1991] proposed that postseismic frictional slip occurs in the rate-strengthening zone (in opposite to the rate-weakening zone for seismicity). *Wang et al.* [2010] suggested that a high population of aftershock activity might change the mechanical property in the fault zone, and that the damage-related inelastic relaxation may contribute to the geodetic measurements. Finally, *Perfettini and Avouac* [2004] proposed that the stress-loading due to afterslip in rate-strengthening zones might produce aftershocks.

[4] The physical understanding of the relations between main shock, aftershocks and postseismic deformation can be improved by detailed investigation of the spatial distribution of aftershocks and inverted coseismic and postseismic slip distributions. Least-square (LS) slip inversions have been commonly used to investigate the time-/space- varying postseismic processes based on observed surface deformations [e.g., *Wang et al.*, 2009; *Ryder et al.*, 2007]. This inversion is to solve the linear system of $\mathbf{y} = \mathbf{Gb}$ so that slip vector ($\mathbf{b}$) on the fault patches projected by Green's function ($\mathbf{G}$) to the observation space has the smallest misfit to the observation vector ($\mathbf{y}$), and meanwhile, the slip values on neighboring fault patches are subject to a smoothing condition. When the observation network is fairly dense and has a good coverage, and the linear system is well constrained, LS method is fast to get solution by simply applying singular value decomposition or QR decomposition to the coefficient matrix of the system. However, Green's function is usually ill-conditioned given large number of discretized fault patches; the inversion is also underdetermined given normally sparse observation network. Therefore, it is already known that inversion solutions are always non-unique and LS results do not provide full information of the solution space. However, the multiplicity of solutions in slip inversion can be conveniently expressed using a Bayesian approach [e.g., *Yabuki and Matsu'ura*, 1992; *Fukuda and Johnson*, 2008, 2010; *Monelli and Mai*, 2008; *Monelli et al.*, 2009]. The Bayesian inversion is formulated in terms of posterior probability density function, which combines the information contained in the data with a priori physical knowledge on the parameters to be estimated. In this study, we adopt the slip inversion in Bayesian approach to investigate spatial correlations among coseismic/postseismic slip and aftershocks.

[5] In particular, we explore the possibility to better constrain slip inversions by taking into account mechanical constraints in the Bayesian framework. We consider possible physical correlations between coseismic/postseismic deformation and aftershocks as prior information. First, the studies focusing on static and dynamic stress triggering indicate that aftershocks mostly locate in the region where Coulomb stress change produced by the main shock is positive [e.g., *King et al.*, 1994; *Toda et al.*, 1998; *Kilb et al.*, 2000; *Felzer and Brodsky*, 2006], although large uncertainty exists in the calculated stress value due to difficulty to precisely invert for the coseismic slip [*Hainzl et al.*, 2009]. Qualitative investigations on spatial correlation indicate that aftershocks mainly locate in the zone where coseismic slip is low and coseismic shear stress change is positive [e.g., *Mendoza and Hartzell*, 1988; *Dalguer et al.*, 2002; *Woessner et al.*, 2006]. Aftershocks distribution has also been thought to be an indication of stress heterogeneity and fault plane heterogeneity in dynamic modeling [e.g., *Helmstetter and Shaw*, 2006; *Karabulut*, 2008]. Therefore, we test the application of the constraint in the slip inversion that coseismic slip has to be separated from aftershocks in space, i.e., aftershocks mainly occur in the zone where coseismic stress change is positive. Second, the two postseismic activities might be correlated physically: aseismic deformation may load its surrounding seismogenic zone [*Perfettini and Avouac*, 2004] and lead to the occurrence of aftershocks (i.e., postseismic creep and aftershocks are disjunct), or aseismic deformation occurs in the same (or surrounding) zone as aftershocks [e.g., *Miyazaki et al.*, 2004; *Ozawa et al.*, 2011], when abundance of aftershocks change the mechanical property in the fault zone [*Lyakhovsky et al.*, 1997] and lead to measureable inelastic deformation [*Wang et al.*, 2010]. Third, considering that geodetically measured aseismic deformation is likely due to stress-driven creep in response to coseismic stress change, we test that postseismic creep is correlated with regions of positive coseismic stress changes. Each physical constraint above is tested in the inversions, and the corresponding slip models are statistically assessed. Based on the physical understanding of the correlations among coseismic rupture, postseismic creep and aftershocks, we do further joint inversions for coseismic and postseismic slip based on GPS measurements and aftershocks data. Finally, our results are shown leading to better constrained and thus probably more accurate inversions of both coseismic and postseismic slip. In this study, we demonstrate the procedure for the case of the 2004 M6.0 Parkfield earthquake.

[6] The 2004 M6.0 Parkfield earthquake was a long-expected event since the last five earthquakes of ~M6.0 periodically occurred with about 22-year recurrence time. Therefore, the Parkfield Earthquake Prediction Experiment was initiated in 1980s, and plenty of instruments including GPS and seismometers were installed long before this 2004 event [*Langbein et al.*, 2006]. Based on the well-instrumented network, the main shock and aftershocks of the 2004 M6.0 event are precisely located, and the postseismic deformation of such a comparably small event was at the first time captured [*Freed*, 2007]. These data provide us a good opportunity to analyze the coseismic and postseismic processes of a strike-slip event [e.g., *Murray and Langbein*, 2006; *Barbot et al.*, 2009; *Bruhat et al.*, 2011]. For example, *Langbein et al.* [2006] inverted from 14 continuous GPS measurements and creepmeter data that the coseismic slip is centered beneath Middle Mountain and ~12 km northwest of the main shock. From the GPS data collected at the same sites, *Freed* [2007] found that the postseismic slip in the first 2 years is above the coseismic rupture, and mostly in the interseismically creeping region where creep rate is reduced prior to the Parkfield event. *Bruhat et al.* [2011] found a complementary location of coseismic and shallow afterslip, and the viscoelastic relaxation in the lower crust with viscosity of 10^{18} Pa·s is needed to fit the long-term GPS measurements (5 years).

[7] In this study, we analyze both the seismic data and the 14 continuous GPS measurements in the Parkfield area (Southern California Integrated GPS Network, SCIGN). The aftershocks of the 2004 Parkfield event have been precisely relocated by *Thurber et al.* [2006] and *Peng and Zhao* [2009]. Based on the 14 continuous GPS measurements in the Parkfield area (Southern California Integrated GPS Network, SCIGN), we invert for coseismic and postseismic

Table 1. Estimated Parameters in Equation (1) for the GPS-Time Series

			N-S components					E-W components				
STN	Lat	Lon	A (mm)	B/(mm)	c (day)	p	RMS[a] (mm)	A (mm)	B (mm)	c (day)	p	RMS[a] (mm)
CAND	35.94	−120.43	58.09	−94.92	0.43	0.92	1.71	−143.29	161.81	1.60	0.96	1.94
CARH	35.89	−120.43	−158.65	139.59	3.53	0.94	2.44	149.62	−126.44	2.37	0.93	2.47
HUNT	35.88	−120.40	114.93	−147.52	0.25	0.95	1.84	−152.89	184.76	1.34	0.96	2.22
MIDA	35.92	−120.46	11.90	−56.75	0.06	0.86	1.66	−75.54	96.32	1.13	0.92	2.37
MNMC	35.97	−120.43	87.34	−118.63	0.78	0.95	1.93	39.84	−64.39	8.58	1.32	1.79
MASW	35.83	−120.44	−138.05	163.77	9.44	0.95	1.83	−60.89	41.11	0.80	1.16	1.97
TBLP	35.92	−120.36	−14.27	−9.37	0.0	0.79	2.41	77.0	−94.80	10.0	1.28	2.41
PKDE	35.94	−120.54	92.33	−99.11	9.67	1.09	1.76	−139.54	104.82	1.36	1.10	1.95
POMM	35.92	−120.48	−85.64	99.46	0.28	0.95	1.97	152.49	−191.46	0.23	0.96	2.11
LAND	35.90	−120.47	−149.52	179.74	1.74	0.96	1.66	−128.11	104.23	1.88	1.12	1.98
HOGS	35.87	−120.48	92.37	−92.37	8.43	1.26	1.65	−127.73	105.87	0.62	1.07	1.93
LOWS	35.83	−120.59	−130.19	130.79	9.81	0.98	1.95	92.11	−103.69	0.46	0.98	1.98
RNCH	35.90	−120.52	61.93	−85.69	7.61	1.32	2.84	−27.28	−10.36	0.0	0.79	2.34
CRBT	35.79	−120.75	3.76	−104.12	32.23	2.06	1.67	−14.33	17.32	2.78	1.53	1.83

[a]RMS is Root-Mean-Square of the modeling residual.

deformation sources with different spatial constraints. The paper is organized into 8 sections. First, we introduce the GPS data and the related time series modeling (Section 2) and the Bayesian inversion approach (Section 3). Then, in Section 4 and 5, we present coseismic and postseismic slip models of the 2004 Parkfield event which are respectively constrained by aftershocks (Section 4) and constrained by stress-condition (Section 5), while the results of the joint inversions integrating both GPS data and aftershock data is shown in Section 6. Finally, we discuss the modeling results in Section 7 and draw our conclusions in Section 8.

2. GPS Data

[8] We utilize the continuous GPS observations at 14 sites (cf. Table 1, Figure 3c) of Southern California Integrated GPS Network (SCIGN) in the Parkfield area. The measurements were started in 2000, and processed in the reference frame of fixed North America plate. Due to the large measurement uncertainty in the vertical components, we only use the horizontal measurements in this study.

[9] The GPS data are first corrected for secular deformation, which is constrained by the measurements of three years before the December 22, 2003, Mw6.5 San Simeon earthquake. This large event occurs ~50 km west to the 2004 Parkfield earthquake. The coseismic motion is shown in the westward direction of ~1 cm in Parkfield region [*Hardebeck et al.*, 2004; *Ji et al.*, 2004; *Rolandone et al.*, 2006]. The postseismic deformation of San Simeon earthquake indicates transient motion with fast decay at the low depth, and therefore, is not significant in the coseismic/postseismic interval of the Parkfield event [*Rolandone et al.*, 2006; *Johanson et al.*, 2006]. After the correction for secular deformation, we calculate the displacements relative to the mean position of each GPS site in 90 days before the Parkfield event. Because we use the daily GPS measurements, the corrected data have ~0 values before the occurrence time of the Parkfield earthquake. The first nonzero values in the day that the Parkfield earthquake occurs provide coseismic displacements (including likely instant postseismic displacements). However, since the measurement uncertainty is different among 14 GPS measurements, we obtain the coseismic and postseismic displacements using the following procedure.

[10] The corrected GPS time series (labeled as $D(t)$) are fitted by the integrated form of Omori-Utsu law, which have been shown to provide good fits in general [*Montési*, 2004; *Wang et al.*, 2010],

$$D(t) = \begin{cases} 0 & t < 0 \\ A + B(t+c)^{1-p} & t \geq 0 \end{cases}, \quad (1)$$

where A, B, c and p are constants. Then, the coseismic displacement can be calculated from $D(0) = A + Bc^{1-p}$ at $t = 0$. We focus in this study the early postseismic processes and only consider the GPS measurements of the first 300 days following the 2004 Parkfield main shock. The parameter estimates for the GPS time series at 14 GPS sites are listed in Table. 1. As an example, Figure 1 shows the modeling results for the GPS time series collected at HUNT site. According to Table 1 and Figure 1, the GPS time series are well modeled by equation (1). Based on the results, we calculate the displacements in different periods, and investigate the coseismic and early postseismic processes.

3. Methodology

[11] Slip inversions in Bayesian approach have been applied in several studies [e.g., *Yabuki and Matsu'ura*, 1992; *Fukuda and Johnson*, 2008]. In the following, we briefly introduce this inversion approach. When neglecting the error in the physical model which is usually unknown, we assume a Gaussian distribution ($N(0, \sigma^2)$) for the error (e) only from the data measurements ($\mathbf{y}$), i.e., e is distributed as $N(0, \sigma^2)$. In this study, we utilize the displacements calculated from GPS time series fitting based on equation (1), and fix σ^2 as 9 mm^2 according to the usually involved error of 2–3 mm in horizontal GPS observations. Then the conditional probability density of $\mathbf{y}$ given slip $\mathbf{b}$ (namely likelihood function) is

$$p(\mathbf{y}|\mathbf{b}) = (2\pi\sigma^2)^{-n/2}\exp\left[-\frac{1}{2\sigma^2}(\mathbf{y}-\mathbf{Gb})^T(\mathbf{y}-\mathbf{Gb})\right], \quad (2)$$

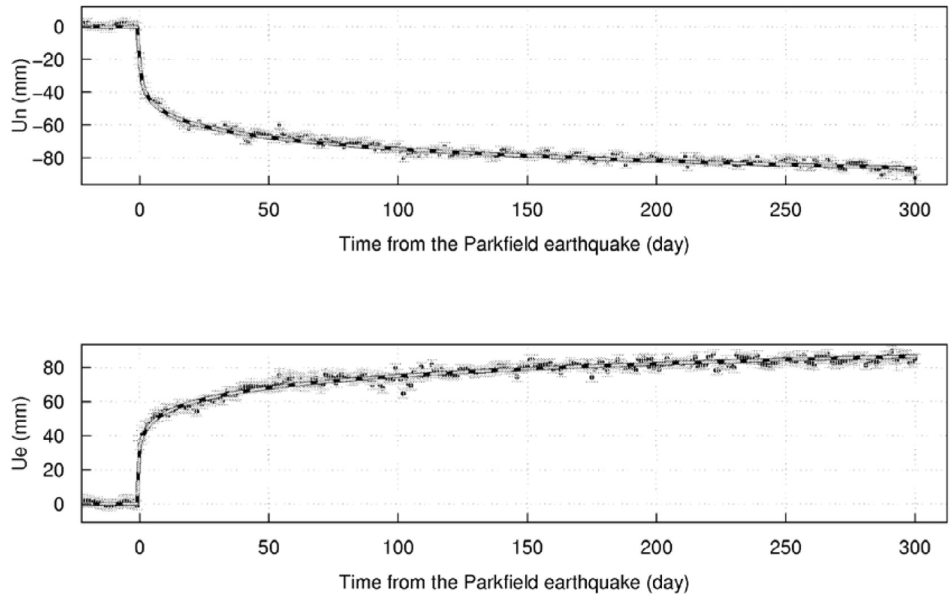

Figure 1. The displacements observed (black dots with error bars) and modeled based on equation (1) (dashed curves) at HUNT site. The displacements with correction for secular component are calculated relative to the position before the 2004 Parkfield earthquake. (top) North component; (bottom) East component.

where **G** is Green's function and n is the number of observations.

[12] Assuming a Gaussian distribution of the slip after applying regularization based on Laplace filter (**L**) [*Reuter et al.*, 2009], $\delta \sim N(0, \alpha^2\mathbf{I})$ with **I** being the identity matrix and α^2 being an unknown parameter that characterizes the distribution of δ, the prior probability density (PDF) of **b** given α^2 is

$$p(\mathbf{b}|\alpha^2) = (2\pi\alpha^2)^{-m/2}\left|\mathbf{L}^T\mathbf{L}\right|^{1/2}\exp\left[-\frac{1}{2\alpha^2}(\mathbf{Lb})^T(\mathbf{Lb})\right], \quad (3)$$

where m is the number of fault patches. According to Bayes' theorem [e.g., *Daston*, 1988], the posterior probability density function is

$$p(\mathbf{b},\alpha^2|\mathbf{y}) \sim p(\mathbf{y}|\mathbf{b},\alpha^2)p(\mathbf{b},\alpha^2) = p(\mathbf{y}|\mathbf{b})p(\mathbf{b}|\alpha^2)p(\alpha^2) \quad (4)$$

In the slip inversion of Bayesian approach, larger α^2 value in equation (4) corresponds to rough slip distribution; while smaller α^2 value provides smoother slip distribution. Since we have no knowledge about α^2, we specify α^2 following a uniform PDF for $\alpha^2 > 0$ m^2. Additionally, we apply positivity constraint to slip **b** for the Parkfield case, so that the slip on all of the fault patches is in right-lateral, i.e., $p(\mathbf{b}, \alpha^2|\mathbf{y}) = 0$) if $b_i < 0$ for all components of **b** ($i = 1,\ldots,m$). To maximize the posterior PDF of equation (4), we can estimate the unknowns $\mathbf{X} = \{\mathbf{b}, \alpha^2\}$. In this study, we use a Markov Chain Monte Carlo (MCMC) method [*Gelfand and Smith*, 1990], to compute the marginal posterior density. Briefly, this method operates in the following way: first, the procedure starts from the initial state $\mathbf{X}_0$ with its posterior $p(\mathbf{X}_0|\mathbf{y})$, second, the new trial value $\mathbf{X}'$ is randomly generated in space ($\mathbf{X}_0 - \Delta\mathbf{X}$, $\mathbf{X}_0 + \Delta\mathbf{X}$)with $\Delta\mathbf{X}$ being the step size of the Markov Chain, and selected as the next state that $\mathbf{X}_1 = \mathbf{X}'$ if $\min(1, \frac{p(\mathbf{X}'|\mathbf{y})}{p(\mathbf{X}_0|\mathbf{y})}) \geq u$, where u is a random number generated from a uniform distribution over the interval [0, 1]. In the same way, the state $\mathbf{X}_2$, $\mathbf{X}_3$… are subsequently generated and selected. After a large number of steps, the procedure converges to the probability density $p(\mathbf{X}|\mathbf{y})$ for any initial state. Finally, a set of samples can be drawn from this posterior PDF.

[13] According to the drawn samples, we can obtain the solutions (and the confidence interval), which have high probability to explain the measurements. Since we apply the positivity constraint to fault slip, its marginal probability density distribution may be asymmetric and truncated at 0 value. The confidence interval of the estimates cannot be obtained straightforwardly. Thus, from the drawn samples, we drop the 2.5% of the samples which are located at each of two sides of the probability density distribution and have low probability value, and specify the 95% confidence interval by the range of values of the remaining samples.

[14] Figure 2a shows the iteration process of MCMC method for the checkerboard test [*Leveque et al.*, 1993] using synthetic data. We utilize the fault geometry provided by C. Ji (http://www.tectonics.caltech.edu/slip_history/2004_ca/parkfield2.html), and the Green's function is constructed in a homogenous half-space [*Okada*, 1992]. This Green's function will be applied to all of the slip models in the later text. The synthetic displacements at the 14 GPS sites of the Parkfield region are simulated from the strike-slip of one meter at the locations indicated by green dots in Figure 3a. We add random values taken from normal distributions with means 0 and standard deviations of 3 mm to account for the noise in the GPS data. The results based on MCMC method indicate that the log-PDF value of the generated samples is relatively stable after 10^6 iterations, suggesting that the system starts from $\sim 10^6$ iterations to converge to the posterior

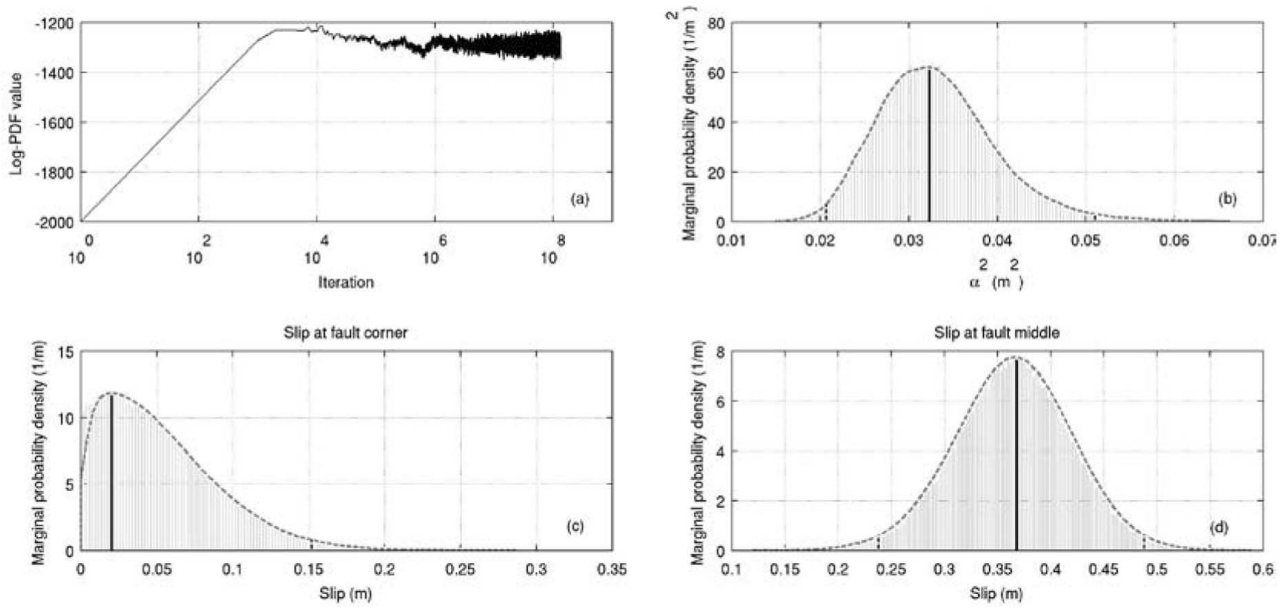

Figure 2. (a) The logarithm of the probability density as a function of the iteration in the case of the checkerboard test. (b) Marginal probability density for parameter α^2 based on $\sim 10^5$ samples. The dashed curve shows the smoothed distribution, the black solid line indicates the preferred value with high probability, and the vertical dashed lines delimitate the 95% confidence interval after excluding 2.5% of the samples with low probability. (c, d) Similar to Figure 2b, plots show the marginal probability density of slip at a fault corner and in the middle of the fault, respectively.

PDF. Therefore, after the first $\sim 10^6$ iterations, we take one sample of the posterior PDF in each 1000 iterations, and get in total $\sim 10^5$ samples. Figure 2b shows the marginal probability density distribution for the α^2 parameter based on the $\sim 10^5$ samples. Figures 2c and 2d show the probability densities for the slip at two fault patches as examples. The

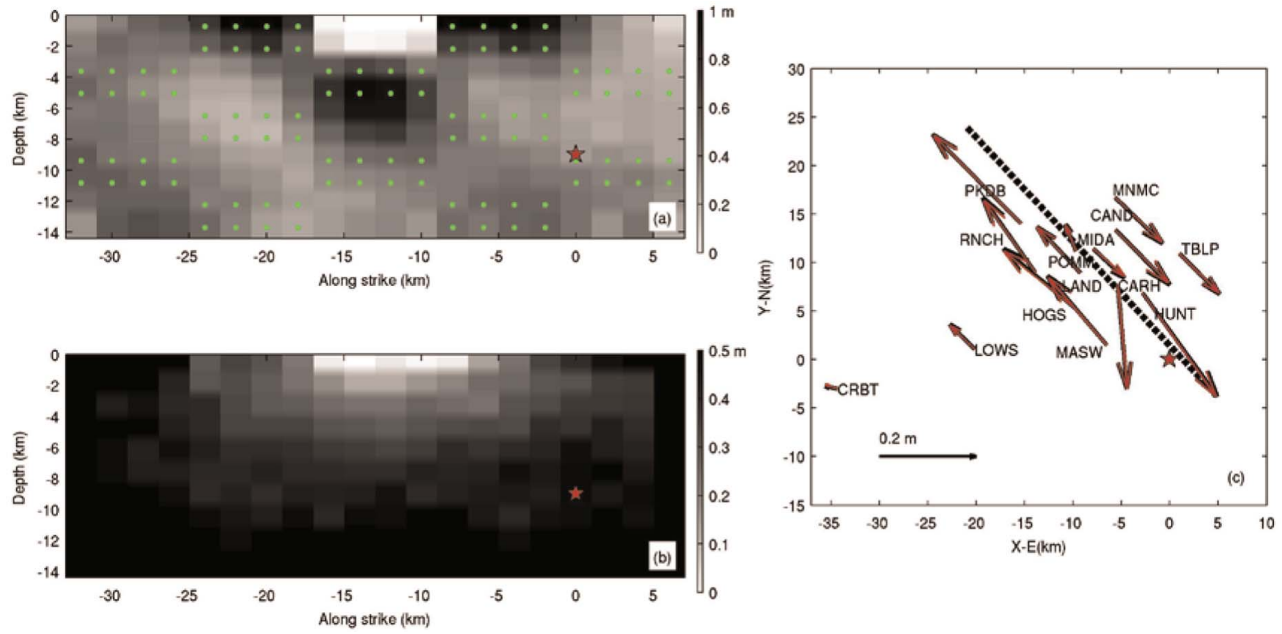

Figure 3. Checkerboard test for the Bayesian slip inversion related to the Parkfield observation network. (a) The input slip model (1-m strike-slip on patches marked by green dots and 0 at all other places) and the inverted slip (in black-white color). (b) The absolute differences between the slip value with the highest probability and the right-side values of the 95% confidence intervals. The red star indicates in both plots the location of the Parkfield main shock. (c) The true (black) and modeled (red) surface displacements at the GPS sites.

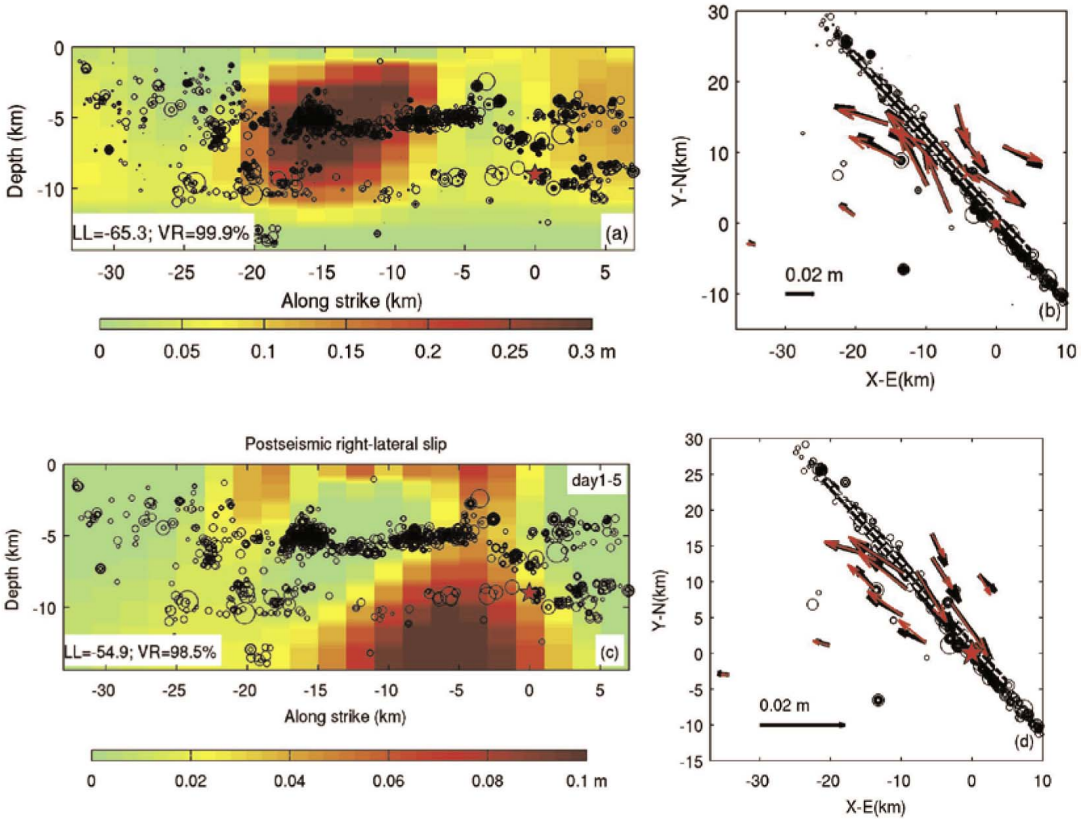

Figure 4. Coseismic and (early) postseismic slip of the 2004 M6.0 Parkfield earthquake derived from Bayesian slip inversion. (a) Color-coded coseismic slip model; (b) observed (black) and modeled (red) coseismic displacements; (c) color-coded postseismic slip model based on the postseismic GPS measurements of day 1–5 following the main shock; (d) observed (black) and modeled (red) postseismic displacements. In Figures 4b and 4d, the black dashed line refers to the location of the fault and the black circles indicate the aftershocks in the first 5 days after the Parkfield event, while the star represents the hypocenter of the Parkfield main shock in Figures 4a and 4c and the epicenter in Figures 4b and 4d.

two patches are exemplary located at the boundary and in the middle of the fault plane, respectively. As seen, the drawn samples provide fairly smooth distributions with unique peak value, indicating that the optimization process converges. Figure 3 shows the inversion result of this checkerboard test. The inversion can in general retrieve the input slip in the area (from −25 km to 0 km along strike and from 0 to 10 km downdip) well covered by the GPS network, while at the two ends of the fault plane, the slip is rather poorly resolved. Thus, in the later applications, the inferred slip at the fault boundary can rarely be trusted. In addition, the Bayesian inversion specifies the confidence interval for each estimate. Figure 3b shows the differences between the optimal values and right-side values of 95% confidence intervals. It indicates much narrower confidence interval for slip in the fault middle than that at the fault boundary. Therefore, the Bayesian inversion provides important information for the resolvability of the slip in each location related to the GPS network, and also provides the full solution space indicated by the optimal slip model and its confidence interval.

[15] Based on the inversion in Bayesian approach, we invert for coseismic slip of the 2004 M6.0 Parkfield earthquake. Since the 2004 Parkfield earthquake is a dominantly strike-slip event, we fix the dip-slip component as 0 in the inversions to decrease the degree of freedom of the model, and only invert for the strike-slip component. During this study, we tested different boundary constraints, such as the inversion with slip taper at the two lateral edges, and at the lower boundary of the fault plane. We found the main inverted slip concentrates in the middle of fault plane, and the inversions with or without the slip taper at the two lateral edges of fault plane provide similar results. We finally only apply the slip taper at the lower boundary of the fault plane. The result is shown in Figure 4. The model with Log likelihood (LL) values of −65.27 can explain 99.9% of the coseismic GPS measurements. Here the percentage is calculated from Variance Reduction: $VR = 1 - \frac{\mathbf{R}^T\Sigma^{-1}\mathbf{R}}{\mathbf{y}^T\Sigma^{-1}\mathbf{y}} \times 100\%$, with $\mathbf{R} = \mathbf{y} - \hat{\mathbf{y}}$, $\hat{\mathbf{y}}$ being the modeling results, and Σ is the covariance matrix of the measurements. Meanwhile, we invert for postseismic slip for the early days (day 1–5) following the 2004 Parkfield main shock. In the inversion for postseismic slip, we relax the slip constraints at the lower boundary of the fault plane, because postseismic relaxation might largely occur at the deep part according to previous

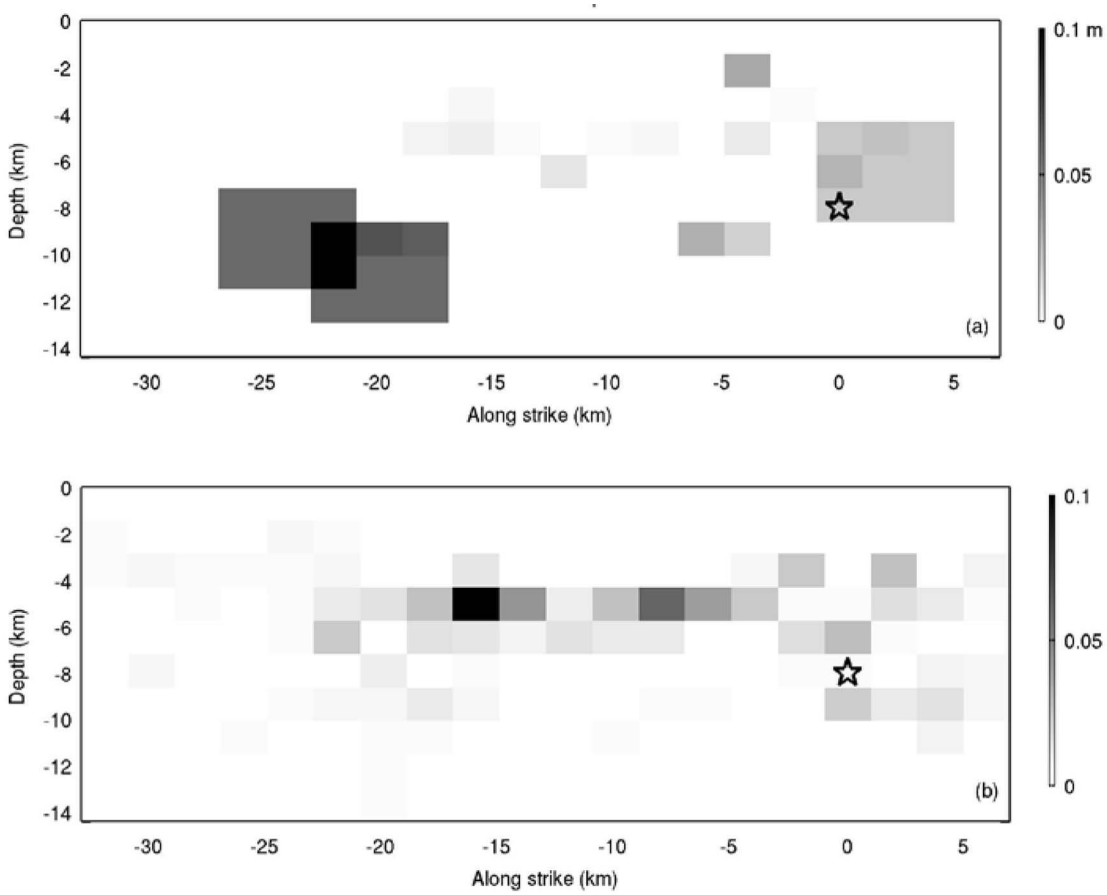

Figure 5. Activity of aftershocks (magnitude larger than 1.0) in the first 5 days after the 2004 Parkfield main shock projected to the coseismic fault plane: (a) cumulative aftershock slip and (b) density. The aftershock-density is normalized to a value between 0 and maximum aftershock-slip. The star indicates the Parkfield hypocenter.

studies [e.g., *Bürgmann et al.*, 2002; *Hsu et al.*, 2007]. The slip model is shown in Figure 4c.

[16] As presented Figure S3 in Text S1 in the auxiliary material, the least squares (LS) inversion of the same data set leads to very similar results indicating the robustness of the Bayesian inversion methodology.[1]

4. Coseismic and Postseismic Slip Model Constrained by Aftershocks

[17] In this section, we investigate spatial correlations between coseismic and postseismic slip and aftershocks, and study the following physical hypotheses: 1) aftershocks are loaded by coseismic rupture, i.e., aftershocks and coseismic slip are spatially separated; 2) aftershocks are loaded by postseismic creep, which suggests that postseismic slip and aftershocks are disjunct; 3) aftershocks occur in the same zone as postseismic creep.

[18] The precisely relocated aftershock distribution of the 2004 M6.0 Parkfield earthquake [*Thurber et al.*, 2006; *Peng and Zhao*, 2009] shows that the aftershocks basically delineate a nearly vertical surface as the fault. We consider the relocated aftershocks in the first 5 days, when the aftershocks intensively occurred. We project the aftershocks (magnitude larger than 1.0) near the fault plane to the coseismic fault plane. We can only find negligible difference between the aftershock data selected in a distance of respectively 3 km, 5 km and 7 km from the fault plane. Therefore, we only show below the results based on the aftershocks in a distance of 5 km from the fault plane which we later apply in the slip inversions. Because the microseismicity and large aftershocks distribute in different areas, we investigate them separately. On one hand, we calculate the rupture area for each aftershock according to the magnitude based on empirical relations [*Wells and Coppersmith*, 1994]. If the calculated rupture area of an aftershock is larger than one patch size, the four patches surrounding the patch where the aftershock locates are also counted as rupture area of this aftershock. Then, based on the approximated rupture area (A), we calculate the slip according to seismic moment by $S/\mu A$, with S being seismic moment calculated from magnitude and μ being shear modulus. Slip distribution produced by aftershocks in the first 5 days following the Parkfield event is shown in Figure 5a. Two major slip zones are outlined: one is near the hypocenter and another one is at

[1]Auxiliary materials are available in the HTML. doi:10.1029/2011JB009017.

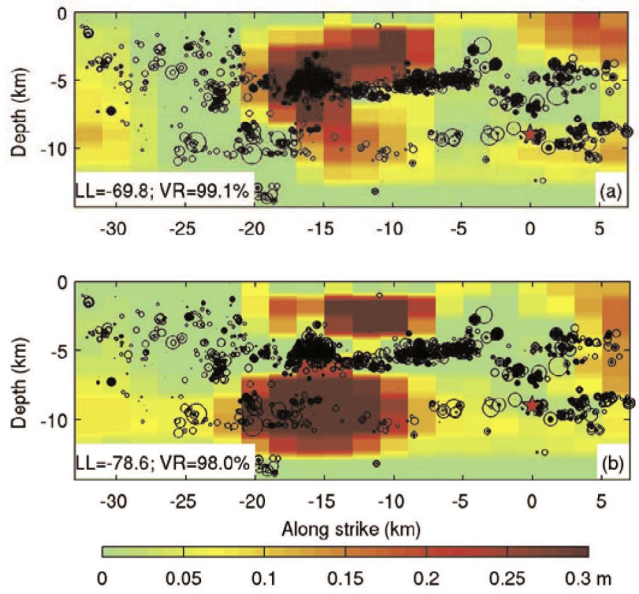

Figure 6. Coseismic slip models constrained by aftershock distribution. The plots show the slip models where coseismic slip is constrained to be separated from (a) aftershock-slip (Model I) and (b) aftershocks-density (Model II). The black dots indicate the aftershocks; the red star represents the Parkfield hypocenter.

the lower-left corner of the main coseismic rupture shown in Figure 4a. We calculate the displacements based on the derived aftershock-slip and find that the aftershocks do not significantly contribute to geodetic measurements (~2%). The aftershock-slip highlights the large events. On the other hand, in order to consider the effect of microseismicity, we calculate the aftershock density projected to each fault patch. Then, the density is normalized to a value between 0 and the maximum value of aftershock-slip. As shown in Figure 5b, a high population of microseismicity is outlined at the ~5 km depth and between −5 and −18 km along strike.

4.1. Coseismic Slip Model Constrained by Aftershocks

[19] Several studies have reported spatial anti-correlations between coseismic slip and aftershock seismicity that aftershocks occur at the highly stressed edges of the rupture zone [*Mendoza and Hartzell*, 1988; *Waldhauser et al.*, 2004]. For the Parkfield event, *Bennington et al.* [2010] presented that the main rupture is primarily between the aftershock 'streaks' at the ~5 km and ~10 km depth. Therefore, we test here how coseismic slip reflected from GPS data is correlated with aftershocks in space. Considering non-uniqueness of the underdetermined inversion problem, we do not directly compare the inverted slip distribution (e.g., Figure 4a) with aftershocks. However, we first take the aftershocks location as prior information (i.e., aftershocks are stress loaded by the main shock, and take place in the separated area from coseismic rupture), and then investigate how an obtained slip model with given prior information explains the GPS data.

[20] We implement the spatial constraints of aftershocks to the prior probability density distribution of equation (3) by modifying the discrete Laplace matrix **L**. The usually applied 2D discrete Laplace filter (D_s^2), which imposes a smoothing condition to slip distribution, is given as

$$D_s^2 = \begin{vmatrix} 1 & 1 & 1 \\ 1 & -8 & 1 \\ 1 & 1 & 1 \end{vmatrix} \quad (5)$$

In order to implement the physical constraints to the slip inversion, we additionally apply the filter (D_c^2) to the related fault patches,

$$D_c^2 = \begin{vmatrix} 1 & 1 & 1 \\ 1 & q^2 & 1 \\ 1 & 1 & 1 \end{vmatrix}. \quad (6)$$

where q^2 is an arbitrary constant larger than 1, and given as 10 in this study. The D_c^2 filter in general depresses the slip on the fault patch that it works on to zero. Large q^2 means strong depressing effect. For example, in the inversion for slip which is assumed to be spatially separated with aftershocks, the filter D_c^2 is applied to the fault patches where aftershocks occurred so that the slip on these patches is close to zero. In this study case, we only consider larger aftershock-slip above 0.01 m, and respectively aftershock-density higher than 0.01. They relate to 29 and 19 fault patches, respectively. The aftershock-related patches mainly locate in the zone that is well covered by the GPS network, and therefore, the aftershock-constraints have influential effects during slip inversions.

[21] The coseismic slip models constrained by aftershock-slip and aftershock-density are shown in Figure 6. Because the large aftershock-slip mainly locates at the border of coseismic slip zone as presented in Figure 4a, the slip model with aftershock-slip constraint (termed as Model I in Table 2) shows a similar distribution as Figure 4a. This model with likelihood value of −69.83 can explain 99.1% (*VR*) of the coseismic GPS measurements. The seismic moment magnitude is 6.0. The slip model constrained by aftershock-density (termed as Model II) is shown in Figure 6b. As expected, the main slip zone is located outside the high (micro-)seismic area. Significant deep (below ~8 km depth) slip is obtained in the model. This model with likelihood value of −78.62 can also fairly well explain the coseismic displacements (*VR* ~ 98.0%). That the two distinctive slip models can similarly well explain the GPS data indicates the limited resolvability of the utilized GPS network and non-uniqueness of the inverted slip model.

4.2. Postseismic Slip Model Constrained by Aftershocks

[22] Both postseismic deformation and aftershocks are important processes following large earthquakes. The two postseismic activities show similar behavior: (1) both have generally consistent kinematic motion with the main shocks [*Bürgmann et al.*, 2002; *Hsu et al.*, 2002; *Bohnhoff et al.*, 2006]; (2) they show similar temporal behaviors [*Perfettini and Avouac*, 2004; *Savage et al.*, 2007; *Perfettini et al.*, 2005; *Hsu et al.*, 2006; *Savage et al.*, 2005; *Perfettini and Avouac*, 2007; *Wang et al.*, 2010]. Therefore, the spatial correlation between aseismic relaxation and aftershocks is very interesting for understanding the physical processes after a large earthquake.

Table 2. Summary of Slip Models

Slip Model	n_p[a]	Slip[b]	Constraints for Slip Model: σ_c	Sign (σ_c)	Separated With Aftershock-Slip	Overlapped With Aftershock-Slip	Separated With Aftershock-Density	Overlapped With Aftershock-Density	*LL*	*VR*	$2n_p$-2*LL*	Figure
0	402	Co.							−65.27	99.9	1044.3	Figure 4a
		Po.							−54.89	98.5		Figure 4b
I	173	Co.			×				−69.83	99.1	485.66	Figure 6a
II	183	Co.					×		−78.62	98.0	523.24	Figure 6b
III	173	Po.			×				−55.12	97.5	456.24	Figure 7a
IV	183	Po.					×		−54.97	97.1	475.94	Figure 7b
V	30	Po.				×			−100.39	37.8	260.78	Figure 7c
VI	20	Po.						×	−94.08	46.3	228.16	Figure 7d
VII	202	Co.							−78.66	98.7	682.14	Figure 9a
		Po.	×						−60.41	90.9		Figure 9c
VIII	312	Co.							−78.66	98.7	895.36	Figure 9a
		Po.		×					−57.02	94.8		Figure 10
IX	173	Co.			×				−84.01	97.1	634.14	Figure 13a
		Po.	×						−60.06	90.9		Figure 13c

[a] n_p refers to the number of free parameters; 'σ_c' refers to shear stress change produced by coseismic slip.
[b] Co. refers to coseismic slip; 'Po.' refers to postseismic slip.

[23] Based on the time series fitting described in Section 2, we investigate the postseismic deformation of day 1–5 following the Parkfield event. The selected time frame is basically consistent with the time interval that aftershocks are considered in this study. Similar to the analysis for coseismic slip model in section 4.1, we invert for the postseismic slip with consideration of aftershock distribution. Figure 7 shows the modeling results for postseismic creep, which is assumed to be separated with aftershock-slip (Model III) and aftershock-density distribution (Model IV), respectively. Both models with likelihood value of ∼−55.0 can explain ∼97% of the measured postseismic displacements during 1–5 days after the Parkfield main shock. The equivalent moment magnitude of the two slip models is ∼5.6. Meanwhile, we also test if the postseismic creep dominantly occurs in the seismic region, that is, postseismic slip overlaps with aftershocks in space. The modeling results constrained by aftershock-slip and aftershock-density (termed as model V and VI) are shown in Figures 7c and 7d, respectively. Since the two slip models have rather low degree of freedom, it is not very surprising that they poorly explain (only ∼40%) the postseismic GPS data.

4.3. Statistical Tests to the Physical Constraints From Aftershocks

[24] The Log likelihood (*LL*) or *VR* values of the physically constrained slip models above indicate their different capabilities to explain GPS data. However, these models have different degrees of freedom, namely ∼30 fault patches with full freedom of slip (the rest ∼170 patches are confined to be zero-slip) for the models assuming that postseismic creep overlaps with aftershocks, while the number of free-slip patches is ∼170 in the cases where coseismic and postseismic slip is assumed to be separated from aftershocks. Therefore, we cannot fairly evaluate the efficiency of the derived models based only on the *LL* (or *VR*) values. Thus,

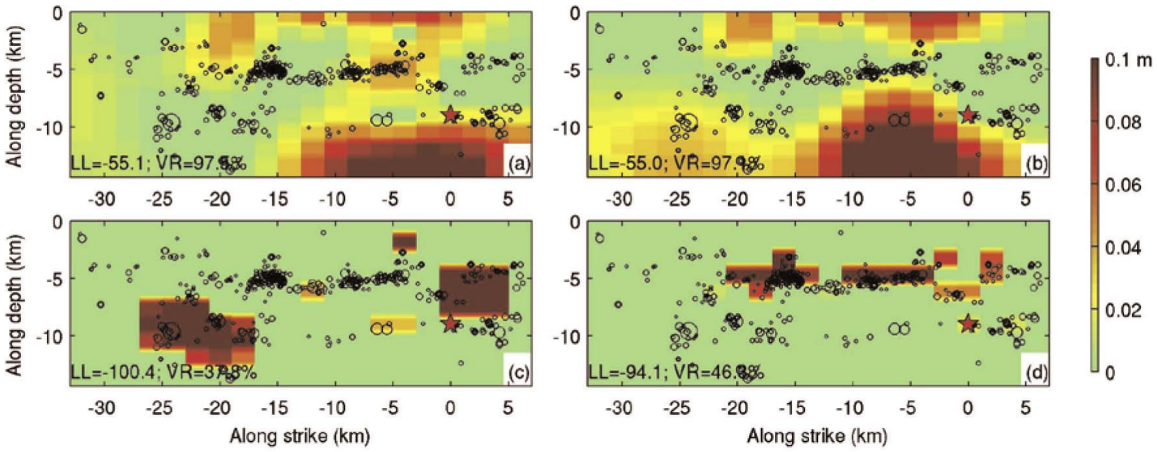

Figure 7. Postseismic slip models for day 1–5 following the 2004 Parkfield main shock, constrained by aftershocks: postseismic slip is (a) spatially separated with higher (≥0.01 m) aftershock-slip zone (Model III in Table 2); (b) separated with higher (≥0.01) aftershock-density zone (Model IV); (c) overlapping with high aftershock-slip zone (Model V); (d) overlapping with high aftershock-density zone (Model VI). The dots indicate the aftershocks and the star represents the Parkfield main shock.

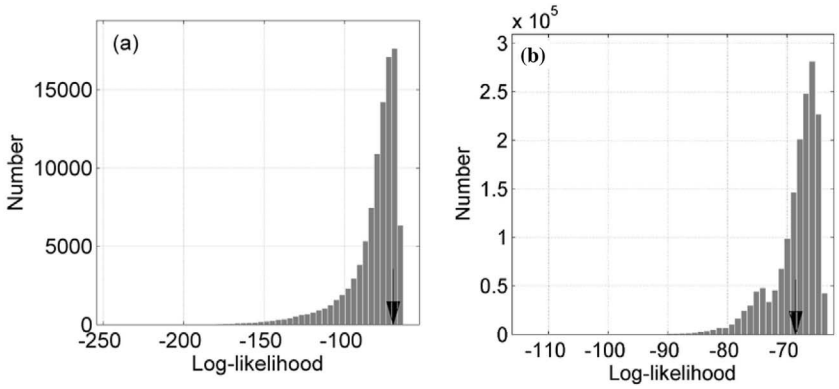

Figure 8. Statistical testing results for the coseismic slip models constrained by the physical assumption that coseismic rupture is separated from large aftershocks and microseismicity, respectively. The plots show *LL* values of 10^6 slip inversions related to the (a) aftershock-slip and (b) aftershock-density constraint, where in each case the locations of allowed slip patches are randomized in space. The black arrow indicates the result of the physically constrained slip model.

we design the following statistical test. For the aftershocks-slip constraint, we first randomize the aftershocks location along the fault plane, and then calculate the aftershocks-slip. In this way, characteristic correlation length relevant to large aftershocks is conserved. For the aftershocks-density constraints, we simply randomize the locations of fault patches that relevant to the high aftershocks-density shown in Figure 5b. For each physical constraint, we generate $\sim 10^6$ random constraints, which have the same number of zero-slip fault patches (or the same number of patches with fully free slip) as the physical constrained model shown in Figures 6 and 7. Then, we invert for $\sim 10^6$ slip models based on the random constraints. Comparing *LL* values between the physically constrained model and the models with random spatial constraints, we can evaluate if the physical assumption is statistically acceptable. Figure 8 shows as examples the statistical tests for the physical constraints that coseismic slip is respectively separated from main aftershock slip and density.

[25] According to Figure 8, the coseismic slip model with the physical constraint that coseismic rupture and large aftershocks are separated, provides larger *LL* value than most (>95%) of the models with randomized locations of the fully free slip. It indicates that this physical constraint is statistically acceptable. On the other hand, the slip model constrained by the assumption that coseismic slip is spatially separated with microseismicity, explains the GPS data worse than most (>50%) of the models with random constraints. Thus, the hypothesis that the coseismic slip is spatially separated from microseismicity is statistically rejected. For the postseismic slip models, the statistical tests (see auxiliary material) in general accept the assumption that postseismic creep is separated from aftershocks, but reject that postseismic creep overlaps with aftershocks.

5. Stress Constrained Coseismic and Postseismic Slip Models

5.1. Inversion Approach

[26] In this section, we test the hypothesis that coseismic and postseismic deformation is correlated by coseismic stress change. Basic considerations lead to the assumption that the postseismic response should be in general proportional to the positive coseismic stress change [*Hainzl et al.*, 2010]. Based on this assumption, we invent a stress-constrained joint inversion for the coseismic slip based on both coseismic and postseismic displacements. The postseismic slip with magnitude $\mathbf{b}_p$ is assumed to be proportional to positive shear stress produced by coseismic slip ($\mathbf{b}_c$),

$$[\mathbf{b}_p]_i = \begin{cases} \beta^2[\mathbf{G}_\sigma \mathbf{b}_c]_i & [\mathbf{G}_\sigma \mathbf{b}_c]_i > 0 \\ 0 & [\mathbf{G}_\sigma \mathbf{b}_c]_i \le 0 \end{cases}, \tag{7}$$

for $i = 1 \ldots m$. In equation (7), β^2 is a scaling factor to stress, $\mathbf{G}_\sigma$ is Green's function to calculate shear stress from slip, and $\mathbf{G}_\sigma \mathbf{b}_c$ provides the coseismic shear stress change. Subscripts 'c' and 'p' in the formula here are used to specify 'coseismic' and 'postseismic', respectively. Thus, the measured postseismic displacement $\mathbf{y}_p$ with uncertainty e_p is assumed to be $\mathbf{y}_p = \mathbf{G}_p \mathbf{b}_p + e_p$, where $\mathbf{G}_p$ is Green's function to relate slip and postseismic observations.

[27] Neglecting the constraint described in equation (7), the joint inversion is to solve $\mathbf{y} = \mathbf{G}\mathbf{b} + e$ with new definitions:

$$\mathbf{G} = \begin{bmatrix} \mathbf{G}_c \\ \beta^2 \mathbf{G}_p \mathbf{G}_\sigma \end{bmatrix}, \quad \mathbf{y} = \begin{bmatrix} \mathbf{y}_c \\ \mathbf{y}_p \end{bmatrix}, \quad e = \begin{bmatrix} e_c \\ e_p \end{bmatrix}. \tag{8}$$

As long as the positivity constraint (equation (7)) is not taken into account, the slip inversion is linear, however, with the positivity constraint for postseismic relaxation (equation (7)), it becomes a nonlinear problem, which can be solved in the framework described in Section 3. Implementing equations (7) and (8) to the likelihood function of equation (2), we have the new likelihood function for the joint inversion,

$$p(\mathbf{y}|\mathbf{b}) = p(\mathbf{y}_c|\mathbf{b}_c,)p(\mathbf{y}_p|\mathbf{b}_c). \tag{9}$$

In equation (9), $p(\mathbf{y}_c|\mathbf{b}_c)$ and $p(\mathbf{y}_p|\mathbf{b}_c)$ basically have the same form as equation (2), but $p(\mathbf{y}_p|\mathbf{b}_c)$ has a new definition for Green's function of $\beta^2 \mathbf{G}_p \mathbf{G}_\sigma$, and has 0 value when $[\mathbf{G}_\sigma \mathbf{b}_c]_i \le$

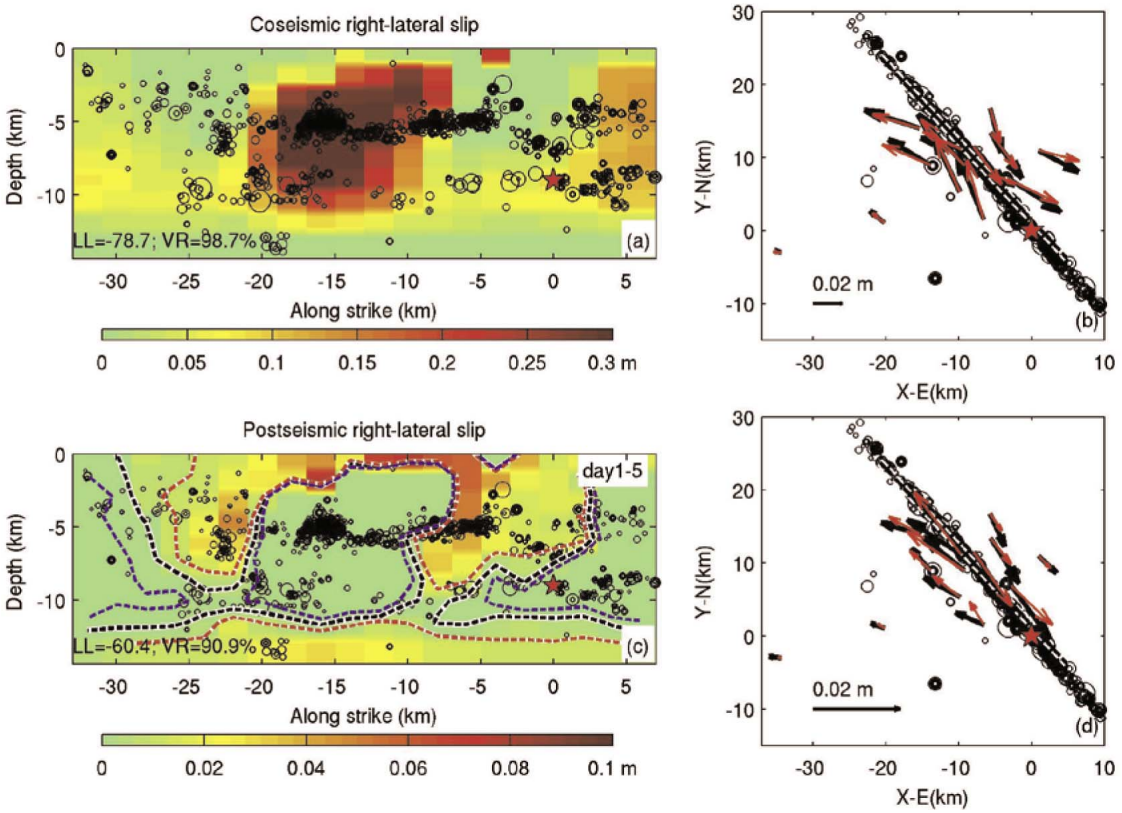

Figure 9. Model VII: Stress-constrained coseismic/postseismic slip model based on coseismic and postseismic (day 1–5) displacements recorded for the Parkfield main shock. The postseismic relaxation is assumed to be proportional to the positive coseismic stress change. (a) Color-coded coseismic slip model; (b) observed (black) and modeled (red) coseismic displacements; (c) color-coded postseismic slip model. The red, black and blue dashed contour lines indicate coseismic shear stress changes of 1.5, 0 and −1.5 bar, respectively; (d) observed (black) and modeled (red) postseismic displacements. The other symbols are the same as those in Figure 4.

0 for $i = 1 \ldots m$. The definition of **y** is given in equation (8). In this joint inversion, we relax the slip taper constraint.

5.2. Stress-Constrained Slip Models

[28] We test the joint inversion for the coseismic slip of the 2004 Parkfield earthquake, based on coseismic displacements together with the postseismic displacements in day 1–5 following the main shock. In this joint inversion, we relax the slip taper at the lower border for the coseismic slip model because positive coseismic stress change (i.e., low or zero coseismic slip) at the deep depth is required in order to produce deep postseismic relaxation and explain the postseismic measurements. Figure 9 shows the derived slip models. Two major coseismic slip zones are obtained from this joint inversion, major slip between −20 km and −10 km along strike and slip near the hypocenter. The estimated moment magnitude is 6.0. The corresponding stress-driven postseismic slip, which is proportional to the positive coseismic stress change, is shown in Figure 9c. As expected, the postseismic slip locates surrounding the coseismic slip. The joint inversion with likelihood value of −139.71 can explain 98.7% of the coseismic displacements and 90.9% of postseismic displacements of day 1–5 following the Parkfield earthquake. This model is termed as Model VII (cf. Table 2).

[29] Although the stress-driven postseismic slip model above can in general explain the GPS observations, the relaxation might be not strictly proportional to the stress due to heterogeneous mechanical property, e.g., space-dependent friction or viscosity. Therefore, we use the coseismic slip model of Figure 9a as known and test the postseismic slip model with spatially varying β_i^2 ($i = 1 \ldots m'$ with m' being the number of fault patches with positive coseismic shear stress change) value in equation (7). In other words, the postseismic slip is not strictly proportional to the positive stress change, but is permitted to vary due to the local rheological properties. Thus, the applied constraint is less strict, and the inversion has more degrees of freedom. The modeling result based on postseismic displacements of day 1–5 is shown in Figure 10 (termed as Model VIII). It indicates that the slip locates in the coseismically stressed area, but slip amount is different from that shown in Figure 9c. This stress-/material-dependent slip model can explain 94.8% of the postseismic GPS measurements, better than the stress-driven model of Figure 9c. Both postseismic slip models show that most of stress relaxation occurs above and below the coseismic slip area, but a large postseismic slip zone also appears in the high seismic area at the depth of 2–8 km.

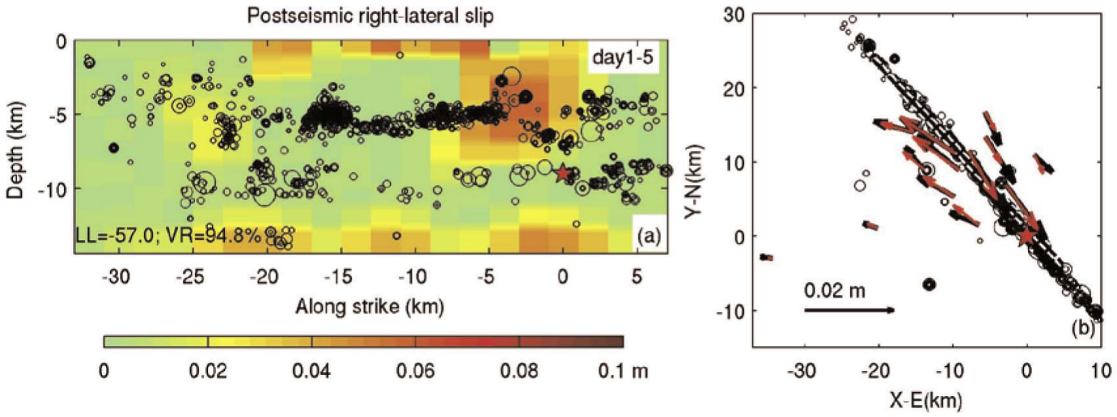

Figure 10. Model VIII: Stress-/material- dependent postseismic slip model for day 1–5 following the Parkfield main shock. (a) Color-coded postseismic slip model and (b) observed (black arrows) and modeled (red arrows) postseismic displacements. The other symbols are the same as those in Figure 4.

[30] Meanwhile, we also test the joint inversions based on the coseismic displacements together with postseismic displacements measured in five other time intervals after the main shock: day 1, day 5–16, day 16–44, day 44–112 and day 112–274. All of the five postseismic intervals have similar amount of displacements as that during day 1–5 (measured by root-sum-square of the displacements). We find that the derived coseismic slip models have generally similar distribution as Figure 9a, and the stress-driven postseismic creep can in general explain more than 85% of the postseismic displacements in the five different periods. The stress-/material- dependent model can overall improve the GPS data fitting and provide increases in Log likelihood (*LL)* values of about 2.0 (except a higher improvement for the first day), as shown in Figure 11. The postseismic deformation in the first day after the Parkfield event is poorly explained by stress-driven model, comparing with the stress-/material- dependent model. It suggests likely different relaxation process immediately after the large event, or that the utilized GPS data with the sampling rate of 1-day is not good enough to resolve the instant 1-day postseismic displacements. The *LL* values of the models for the first half-month is higher than the later time periods, indicating likely time-varying stress field. For example, *Bruhat et al.* [2011] suggested that viscoelastic relaxation in the lower crust might contribute to the observed postseismic displacements. This deep relaxation has increasing impact in the later postseismic interval, and might then become influential to the stress field.

5.3. Statistical Test of the Stress-Constrained Results

[31] Similar as the statistical tests to the aftershock-constraints to coseismic/postseismic slip models, we evaluate here the physical hypothesis that postseismic slip is

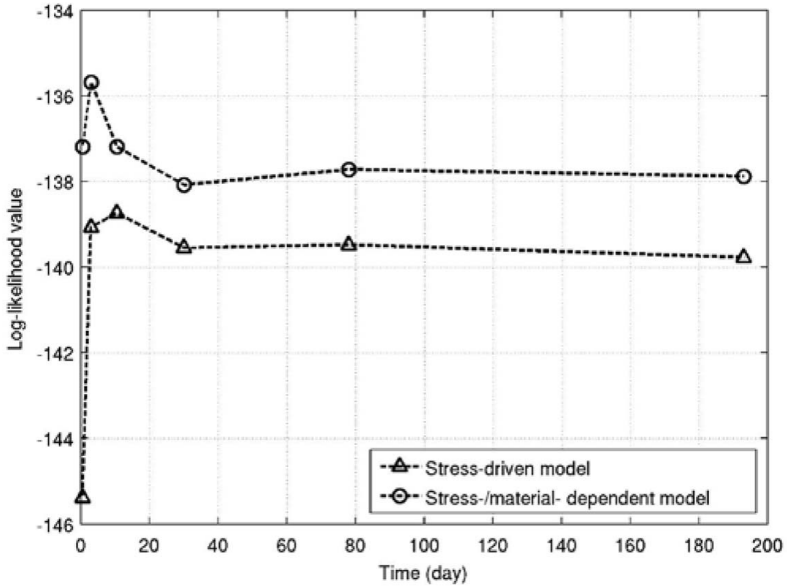

Figure 11. Log likelihood values of slip models resulting from stress-constrained joint inversions.

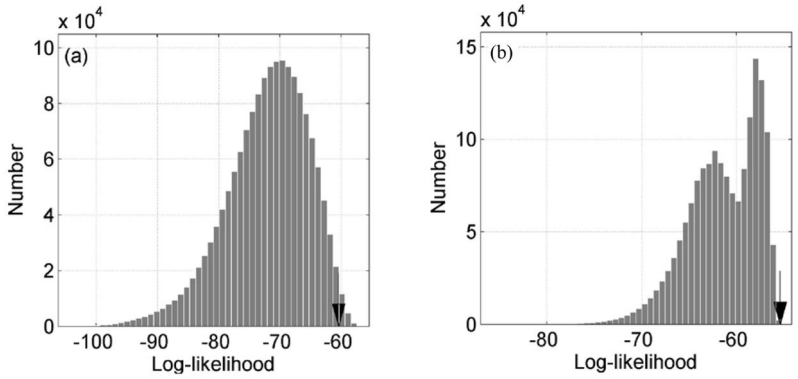

Figure 12. Statistical tests to the physical hypothesis that postseismic slip is triggered by coseismic stress perturbations for (a) linear correlation between stress and postseismic slip and (b) stress-/material- dependent postseismic slip. Histograms show *LL* values of the models with randomized spatial constraints, and the black arrow indicates the *LL* value of the physically constrained model.

predominantly due to coseismic stress perturbation. For the stress-driven model (i.e., postseismic creep is assumed to be proportional to positive coseismic stress change), we design the following statistical test. Given the coseismic slip model as Figure 9a, we know the coseismic stress distribution. We test now whether the spatial distribution based on the physical reasoning is decisive for the quality of the fit or whether similar results can be achieved by applying similar constraints without physical reasoning. For that, we randomize the stress distribution, and recalculate the least squares solution of β^2 in equation (7) to best fit to the postseismic displacements. We repeat such calculations based on $\sim 10^6$ randomized stress distributions, and compare the *LL* values with the *LL* value of the physically constrained model. As shown in Figure 12a, the physical model has a higher *LL* value than at least 95% of the models with random constraints, indicating the validity of the physical assumption with high statistical significance.

[32] We also do the test also for the stress-/material-dependent postseismic slip model. According to the coseismic slip model provided in Figure 9a, 110 fault patches are stressed by the main shock. For this test, we randomize the spatial distribution of 110 fault patches on the fault plane (200 patches in total and invert for postseismic slip in day 1–5 following the Parkfield earthquake. The *LL* values of models based on $\sim 10^6$ randomizations are shown in Figure 12b. Our result indicates that the physically constrained slip model (displayed by black arrow in Figure 12b) has larger *LL* value than most (>95%) randomized models. Both tests indicate that the stress-related physical correlation between coseismic slip and postseismic creep is statistically significant.

6. Stress- and Aftershock-Constrained Joint Inversion

[33] According to investigations in Section 4 and 5, the physical assumptions that postseismic creep and large aftershocks are driven by the main shock are statistically significant and can explain the GPS measurements in general. In this section, we join both assumptions and test joint slip-inversions based on coseismic and postseismic GPS measurements with stress- and aftershock-constraints. The postseismic displacements are modeled by stress-driven creep in response to coseismic stress perturbation, and large aftershocks are assumed to define locations of positive changes in shear stress due to the main shock and thus locate outside the coseismic rupture zone.

[34] The construction of the posterior PDF of this joint slip inversion is based on the likelihood function described by equation (9), and the prior PDF with modified Laplace filter is described in section 4.1. As before, only larger aftershocks-slip (≥0.01 m) is taken into account during the inversion. We utilize the postseismic displacements occurred between day 1–5. The results are shown in Figure 13. The slip model derived from coseismic/postseismic displacements and aftershocks-slip distribution (Model IX) provides a likelihood value of −144.07 and can explain 97.1% and 90.1% of the coseismic and postseismic displacements, respectively. The estimated moment magnitude of the main shock is 5.9. The uncertainty according to 95% confidence interval (similar as the uncertainty shown in Figure 3b) of the inverted coseismic slip of Figure 13a is provided in Figure 13b. Because low degree of freedom is given to the slip patches with large aftershocks-slip during the inversion, the inverted coseismic slip in such zone has narrow uncertainty.

7. Discussion

7.1. Inversion Method and Slip Models

[35] In this study, we apply slip inversions in Bayesian approaches and Markov Chain Monte Carlo method to obtain fault slip from geodetic measurements and seismicity data. Comparing with the normally used Least-Square inversion, this method is able to be used for solving a nonlinear problem with an uncertainty assessment. Formulated in the concept of probability, the Bayesian inversion approach provides an optimal weighting factor (α^2) to slip regularization, because either too large or too small weighting factor produces lower probability density of equation (3). The checkerboard test indicates that our applied inversion can basically retrieve the input slip model with relatively narrow confidence interval in the fault middle, where it is well covered by the GPS network. The resolvable region of the GPS network is roughly

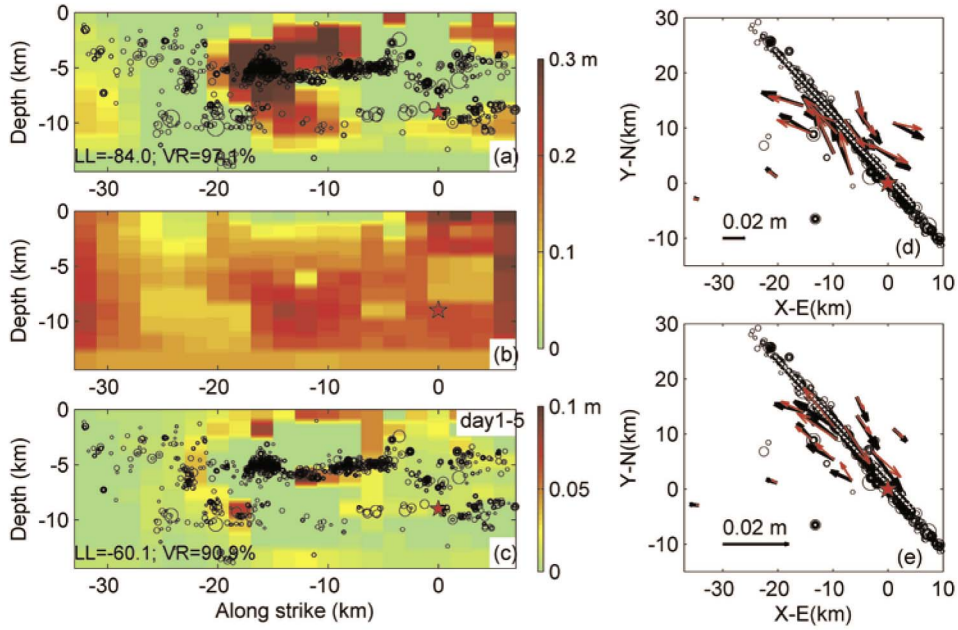

Figure 13. Model IX: Slip models constrained by coseismic and postseismic GPS measurements together with aftershock-slip (≥0.01 m). (a) Color-coded coseismic slip model; (b) uncertainty (similar as Figure 3b) of slip in Figure 13a; (c) color-coded postseismic slip model; (d) observed (black) and modeled (red) coseismic displacements; (e) observed (black) and modeled (red) postseismic displacements of day 1–5 following the Parkfield main shock. The other symbols are the same as those in Figure 4.

between −25 and 5 km along strike (relative to the Parkfield hypocenter) and above 10 km depth.

[36] In this study, we adopted the fault geometry given by C. Ji (http://www.tectonics.caltech.edu/slip_history/2004_ca/parkfield2.html), which is well consistent with aftershock distribution. Our Green's function applied in the slip inversion is based on half-space, neglecting lateral heterogeneity (e.g., bimaterial) across the fault plane that has been reported in the Parkfield region [*Boness and Zoback*, 2004; *Zhao et al.*, 2009]. Such treatment might bring some bias in the slip modeling. This bimaterial effect will be discussed in details in a separated section (7.2). Our derived coseismic slip model based on half-space Green's function (e.g., Figure 4a) shows two major coseismic slip zones: the main slip at 10–20 km northwest to the hypocenter and slip around the hypocenter. Both are located at the depth of ∼4–10 km. The obtained major slip is similar as those presented in other studies [e.g., *Langbein et al.*, 2006; *Barbot et al.*, 2009] based on geodetic measurements, indicating the reliability of our adopted slip inversion method.

[37] Based on the Bayesian inversion approach, we have tested several physical assumptions: (1) large aftershocks define locations which are stress-loaded by the main shock; (2) microseismicity is stress-loaded by the main shock; (3) geodetically measured postseismic deformation is due to creep triggered in regions with positive main shock-induced stress changes; (4) aftershocks might be stress-loaded by postseismic creep; (5) aftershocks may occur in the same area as postseismic creep. Statistical tests for the 2004 Parkfield earthquake show that the physical assumptions 1, 3 and 4 are in general accepted, while the second and fifth assumptions are rejected. Therefore, our tests indicate that both aftershocks and postseismic creep locate outside area of the coseismic rupture, indicating that both are stress-driven by the 2004 Parkfield main shock which occurred in a *transition zone* between the central creeping segment to the northwest and the *locked* segment to the southeast [*King et al.*, 1987]. This is different from the reported postseismic activities following the 2011 M9.1 Tohoku earthquake in Japan. The postseismic creep and aftershocks of the Tohoku earthquake are overlapping with the coseismic rupture [*Ozawa et al.*, 2011]. The fitting results (*LL* and *VR* values) of all tested joint inversions are summarized in Table 2.

[38] Comparing the joint slip models (0, VII, VIII and IX) in Table 2, we see that model 0 or model VIII (stress-/material-dependent model) with the larger *LL* (or *VR*) value seems better to explain the GPS observations than the other joint models. However, both of the models have much more free parameters n_p than the others. Similar as Akaike information criterion [*Akaike*, 1970], we calculate $2n_p$-$2LL$ for each slip model, which is also listed in Table 2. As seen, the improvement in *LL* value of model 0 (or VIII) is largely balanced by the large number of the free parameters. Therefore, considering both the degree of freedom and the goodness of the model fitting the GPS observations, model IX appears the most efficient to explain both GPS and aftershock measurements in the sense of information criteria. The results indicate that the early major postseismic processes (including aseismic deformation and large aftershocks) of the 2004 Parkfield earthquake can be basically explained by stress relaxation in response to coseismic stress change. The negligible *LL* difference between stress-driven postseismic creep (model VII) and stress-/material dependent postseismic creep (model VIII) indicates that material heterogeneity has not to be taken into account for describing the early postseismic relaxation process. Furthermore, the

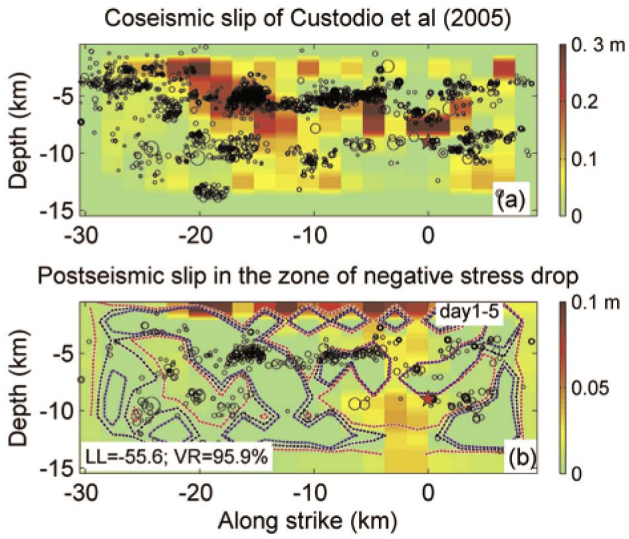

Figure 14. (a) Color-coded coseismic slip of *Custódio et al.* [2005] based on strong motion data and (b) postseismic slip of day 1–5 following the main shock, constrained by coseismic stress change based on slip in Figure 14a. In Figure 14b, the blue, black and red contour lines mark respectively the coseismic shear stress changes of 1.5, 0 and −1.5 bar based on slip in Figure 14a. The other symbols are the same as those in Figure 4.

modeling results for the 2004 Parkfield earthquake show that the postseismic displacements in the first half month can better been explained by stress-driven model than that in the later time periods.

[39] So far, our inversions are only based on geodetic surface measurements. Generally, studies based on strong motion data can provide better resolution at the larger depth (>10 km) than results based on GPS data [*Custódio et al.*, 2005; *Liu et al.*, 2006]. As an example, the coseismic Parkfield slip model of *Custodio et al.* [2005] shown in Figure 14a resolves more heterogeneous slip than the models based on GPS data. Utilizing the same approach for model VIII, we invert for postseismic slip (for day 1–5 following the main shock) constrained by stress change of coseismic slip of Figure 14a. The result is presented in Figure 14b. The model can explain ∼96% of postseismic displacements, indicating high correlation between postseismic creep and positive coseismic stress change, although different type of coseismic data is considered. Figure 14 also indicates that larger aftershocks mainly locate in the zone loaded by the main shock, while most of microseismicity locate in the zone of coseismic rupture. This is consistent with the results based only on GPS data. This result leads to the conclusion that it will be worthwhile to extend our approach to joint inversions including strong motion data in the future.

7.2. Bimaterial Reflected From Postseismic Geodetic Measurements Following the 2004 Parkfield Event

[40] The geodetic observations of the 2004 Parkfield event show asymmetric postseismic relaxation at the two sides of the fault trace. According to Figure 9d or Figure 10b, the results basically fit the recorded postseismic displacements on southwest side of the fault well, but overall underestimate the deformation observed on the northeast side. The modeling errors (projected along the direction of motion) of the slip model shown in Figure 10b are plotted in Figure 15a. As seen, the modeled displacements on the east side are mostly smaller than the observations, and the differences are larger than the usual GPS measurement uncertainty of 2–3 mm. Similar behavior is also observed from the slip models derived from LS inversion (Figure S5 in Text S1 in the auxiliary material). It indicates that the relaxation on the east side of the fault is faster than the southwest side, and

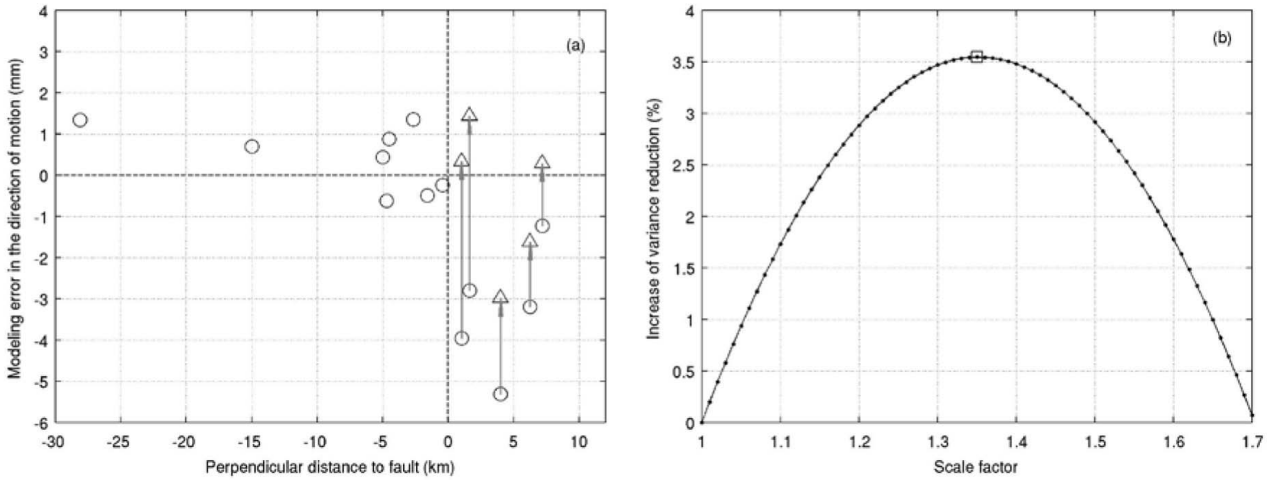

Figure 15. (a) Modeling errors (based on Figure 10) at each GPS site are plotted against the perpendicular distance of the site to fault, and are shown by circles. The positive distance values correspond to the east side of the fault. (b) Improvement in *VR* value is plotted against scaling factor (χ), characterizing material contrast ratio between east and west side of the fault. The material contrast of 1.35 can improve the data fitting by 3.5%. The remaining modeling errors after consideration of the material contrast (1.35) are indicated by triangles in plot Figure 15a.

produce relatively larger postseismic displacements in early days after the Parkfield event.

[41] The asymmetric postseismic displacements are not expected for a vertical strike-slip fault provided that the Earth's crust is transversely homogeneous and isotropic. Thus it might indicate an across-fault contrast of the host rocks [*Lisowski et al.*, 1991]. For the postseismic period, when coseismic stress $\boldsymbol{\sigma}_c$ is given according to coseismic slip $\mathbf{b}_c$, the strain $\boldsymbol{\varepsilon}_p$ (subscribe 'p' specifying 'postseismic') in response to the coseismic stress perturbation is $\boldsymbol{\sigma}_c/\mu$, with μ being the effective shear modulus. Now we assume that the rock at the east and west side of fault is different, and has effective shear modulus μ_W and μ_W/χ respectively, where χ is the scaling factor describing the ratio of the contrast in effect shear modulus. Then, the produced strain is asymmetric at the two sides of the fault with a strain ratio ($\boldsymbol{\varepsilon}_{p,E}/\boldsymbol{\varepsilon}_{p,W}$) of χ. In our slip model, where the postseismic stress relaxation is simulated as creep-like slip, the asymmetric strain at east side can be expressed as

$$[\mathbf{b}_{p,E}]_i = \chi[\mathbf{b}_{p,W}]_i = \begin{cases} \chi\beta^2[\mathbf{G}_\sigma\mathbf{b}_c]_i & [\mathbf{G}_\sigma\mathbf{b}_c]_i > 0 \\ 0 & [\mathbf{G}_\sigma\mathbf{b}_c]_i \le 0 \end{cases} \text{ for } i = 1\ldots m.$$

Based on the postseismic displacements of day 1–5 following the Parkfield event, we find that χ of ~1.35 improves the model fitting by 3.5% (see Figure 15). The contrast ratio of ~1.35 in shear modulus corresponds to the contrast ratio of ~1.15 in seismic velocity according to $\mu = V_s^2\rho$ with V_s being the S-wave velocity and ρ being the density. This is consistent with geological and geophysical observations. For example, the crustal structure across the San Andreas Fault from drilling data near the rupture zone of the 2004 Parkfield earthquake shows that the seismic velocity on the west side is 10–25% faster than the east side at the seismogenic depth [*Boness and Zoback*, 2007]. Detailed seismological studies [*Zhao et al.*, 2009] in this region show an average velocity difference of ~4–10% near the main rupture of the 2004 Parkfield event, and the material contrast is even stronger at the lower depth.

8. Conclusions

[42] Slip inversions are known to be generally non-unique. In this study, we utilize the Bayesian inversion approach to obtain slip distributions in a probabilistic formulation and make use of our physical process understanding of the main shock, aftershock and postseismic creep generation to constrain the inversions. In particular, we developed a joint inversion approach for coseismic and postseismic slip based on coseismic and postseismic GPS measurements and aftershock data and test the joint inversion to the 2004 M6.0 Parkfield earthquake. The results show that early postseismic displacements following the main shock (in the first year) can be in principal explained by stress-driven creep in response to coseismic stress perturbations, and the large aftershocks locates in the zone loaded by the main shock. Thus, postseismic activities (including aseismic relaxation and large aftershocks) can be reasonably explained by stress relaxation processes. Our results also indicate that the data for constraining coseismic slip could be enriched postseismically, especially based on geodetic measurements in the first month following the main shock. In addition, the postseismic displacements in the Parkfield area also show asymmetric relaxation processes at two sides of the fault. The stress relaxation on northeast side of the fault is faster and produces larger deformation than that on the southwest side. It suggests different materials at the two side of the fault. A material contrast ratio of ~1.35 in effective shear modulus (~1.15 in seismic velocity) is obtained based on the early postseismic displacements following the 2004 Parkfield earthquake. The obtained material contrast ratio is consistent with geological and geophysical observations.

[43] **Acknowledgments.** We are grateful to the Associate Editor, Hugo Perfettini and an anonymous reviewer for their work and the excellent reviews which helped us a lot to improve the manuscript. We thank Zhigang Peng for providing us the aftershock catalog. The fault data were obtained from Finite-Source Rupture Model Database maintained by Martin Mai. This work is supported by PROGRESS project.

References

Akaike, H. (1970), Statistical predictor identification, *Ann. Inst. Stat. Math.*, *22*, 203–217, doi:10.1007/BF02506337.

Barbot, S., Y. Fialko, and Y. Bock (2009), Postseismic deformation due to the Mw 6.0 2004 Parkfield earthquake: Stress-driven creep on a fault with spatially variable rate-and-state friction parameters, *J. Geophys. Res.*, *114*(B7), B07405, doi:10.1029/2008JB005748.

Bennington, N., C. Thurber, K. Feigl, and J. Murray-Moraleda (2010), Aftershock distribution as a constraint on the Geodetic model of coseismic slip for the 2004 Parkfield earthquake, *Pure Appl. Geophys.*, *168*, 1553–1565.

Bohnhoff, M., H. Grosser, and G. Dresen (2006), Strain partitioning and stress rotation at the North Anatolian fault zone from aftershock focal mechanisms of the 1999 Izmit Mw = 7.4 earthquake, *Geophys. J. Int.*, *166*(1), 373–385, doi:10.1111/j.1365-246X.2006.03027.x.

Boness, N. L., and M. D. Zoback (2004), Stress-induced seismic velocity anisotropy and physical properties in the SAFOD Pilot Hole in Parkfield, CA, *Geophys. Res. Lett.*, *31*, L15S17, doi:10.1029/2003GL019020.

Boness, N. L., and M. D. Zoback (2007), A multiscale study of the mechanisms controlling shear velocity anisotropy in the San Andreas Fault Observatory at Depth, *Geophys. Prospect.*, *71*(5), 131–146.

Bruhat, L., S. Barbot, and J.-P. Avouac (2011), Evidence for postseismic deformation of the lower crust following the 2004 Mw6.0 Parkfield earthquake, *J. Geophys. Res.*, *116*, B08401, doi:10.1029/2010JB008073.

Bürgmann, R., P. Segall, M. Lisowski, and J. Svarc (1997), Postseismic strain following the 1989 Loma Prieta earthquake from GPS and leveling measurements, *J. Geophys. Res.*, *102*, 4933–4955, doi:10.1029/96JB03171.

Bürgmann, R., S. Ergintav, P. Segall, E. H. Hearn, S. McClusky, R. E. Reilinger, H. Woith, and J. Zschau (2002), Time-dependent distributed afterslip on and deep below the İzmit earthquake rupture, *Bull. Seismol. Soc. Am.*, *92*(1), 126–137, doi:10.1785/0120000833.

Custódio, S., P. Liu, and R. J. Archuleta (2005), The 2004 Mw6.0 Parkfield, California, earthquake: Inversion of near-source ground motion using multiple data sets, *Geophys. Res. Lett.*, *32*, L23312, doi:10.1029/2005GL024417.

Dalguer, L. A., K. Irikura, W. Zhang, and J. D. Riera (2002), Distribution of dynamic and static stress changes during 2000 Tottori (Japan) earthquake: Brief interpretation of the earthquake sequences; foreshocks, mainshock and aftershocks, *Geophys. Res. Lett.*, *29*(16), 1758, doi:10.1029/2001GL014333.

Daston, L. (1988), *Classical Probability in the Enlightenment*, Princeton Univ. Press, Princeton, N. J.

Dieterich, J. H. (1994), A constitutive law for rate of earthquake production and its application to earthquake clustering, *J. Geophys. Res.*, *99*, 2601–2618, doi:10.1029/93JB02581.

Dieterich, J. H., and B. Kilgore (1996), Implications of fault constitutive properties for earthquake prediction, *Proc. Natl. Acad. Sci. U. S. A.*, *93*, 3787–3794, doi:10.1073/pnas.93.9.3787.

Ellsworth, W. L., and G. C. Beroza (1995), Seismic evidence for an earthquake nucleation phase, *Science*, *268*(5212), 851–855, doi:10.1126/science.268.5212.851.

Felzer, K. R., and E. E. Brodsky (2006), Decay of aftershock density with distance indicates triggering by dynamic stress, *Nature*, *441*(7094), 735–738, doi:10.1038/nature04799.

Freed, A. M. (2007), Afterslip (and only afterslip) following the 2004 Parkfield, California, earthquake, *Geophys. Res. Lett.*, *34*, L06312, doi:10.1029/2006GL029155.

Fukuda, J., and K. M. Johnson (2008), A fully Bayesian inversion for spatial distribution of fault slip with objective smoothing, *Bull. Seismol. Soc. Am.*, *98*(3), 1128–1146, doi:10.1785/0120070194.

Fukuda, J., and K. M. Johnson (2010), Mixed linear-non-linear inversion of crustal deformation data: Bayesian inference of model, weighting and regularization parameters, *Geophys. J. Int.*, *181*, 1441–1458.

Gelfand, A. E., and A. F. M. Smith (1990), Sampling-based approaches to calculating marginal densities, *J. Am. Stat. Assoc.*, *85*, 398–409.

Hainzl, S., B. Enescu, M. Cocco, J. Woessner, F. Catalli, R. Wang, and F. Roth (2009), Aftershock modeling based on uncertain stress calculations, *J. Geophys. Res.*, *114*, B05309, doi:10.1029/2008JB006011.

Hainzl, S., G. B. Brietzke, and G. Zöller (2010), Quantitative earthquake forecasts resulting from static stress triggering, *J. Geophys. Res.*, *115*, B11311, doi:10.1029/2010JB007473.

Hardebeck, J. L., et al. (2004), Preliminary report on the 22 December 2003 M6.5 San Simeon, California, earthquake, *Seismol. Res. Lett.*, *75*, 155–172, doi:10.1785/gssrl.75.2.155.

Helmstetter, A., and B. E. Shaw (2006), Relation between stress heterogeneity and aftershock rate in the rate-and-state model, *J. Geophys. Res.*, *111*, B07304, doi:10.1029/2005JB004077.

Hsu, Y.-J., N. Bechor, P. Segall, S.-B. Yu, L.-C. Kuo, and K.-F. Ma (2002), Rapid afterslip following the 1999 Chi-Chi, Taiwan earthquake, *Geophys. Res. Lett.*, *29*(16), 1754, doi:10.1029/2002GL014967.

Hsu, Y.-J., M. Simons, J.-P. Avouac, J. Galetzka, K. Sieh, M. Chlieh, D. Natawidjaja, L. Prawirodirdjo, and Y. Bock (2006), Frictional afterslip following the 2005 Nias-Simeulue earthquake, Sumatra, *Science*, *312*, 1921–1926.

Hsu, Y.-J., P. Segall, S.-B. Yu, L.-C. Kuo, and C. A. Williams (2007), Temporal and spatial variations of post-seismic deformation following the 1999 Chi-Chi, Taiwan earthquake, *Geophys. J. Int.*, *169*(2), 367–379, doi:10.1111/j.1365-246X.2006.03310.x.

Ji, C., K. M. Larson, Y. Tan, K. W. Hudnut, and K. Choi (2004), Slip history of the 2003 San Simeon earthquake constrained by combining 1-Hz GPS, strong motion, and teleseismic data, *Geophys. Res. Lett.*, *31*, L17608, doi:10.1029/2004GL020448.

Johanson, I. A., E. J. Fielding, F. Rolandone, and R. Bürgmann (2006), Coseismic and postseismic slip of the 2004 Parkfield earthquake from space-geodetic data, *Bull. Seismol. Soc. Am.*, *96*(4B), S269–S282, doi:10.1785/0120050818.

Karabulut, M. B. H. (2008), The aftershock signature of supershear earthquakes, *Science*, *320*, 1323–1325.

Khazaradze, G., and J. Klotz (2003), Short- and long-term effects of GPS measured crustal deformation rates along the south central Andes, *J. Geophys. Res.*, *108*(B6), 2289, doi:10.1029/2002JB001879.

Kilb, D., J. Gomberg, and P. Bodin (2000), Triggering of earthquake aftershocks by dynamic stresses, *Nature*, *408*(6812), 570–574, doi:10.1038/35046046.

King, G. C. P., R. S. Stein, and J. Lin (1994), Static stress changes and the triggering of earthquakes, *Bull. Seismol. Soc. Am.*, *84*, 935–953.

King, N. E., P. Segall, and W. Prescott (1987), Geodetic measurements near Parkfield, California, 1959–1984, *J. Geophys. Res.*, *92*, 2747–2766, doi:10.1029/JB092iB03p02747.

Langbein, J., J. R. Murray, and H. A. Snyder (2006), Coseismic and initial postseismic deformation from the 2004 Parkfield, California, earthquake, observed by global positioning system, electronic distance meter, creepmeters, and borehole strainmeters, *Bull. Seismol. Soc. Am.*, *96*(4B), S304–S320, doi:10.1785/0120050823.

Leveque, J. J., L. Rivera, and G. Wittlinger (1993), On the use of the checkerboard test to assess the resolution of tomographic inversions, *Geophys. J. Int.*, *115*, 313–318, doi:10.1111/j.1365-246X.1993.tb05605.x.

Lisowski, M., J. C. Savage, and W. H. Prescott (1991), Velocity field along the San Andreas fault in central and southern California, *J. Geophys. Res.*, *96*(B5), 8369–8389, doi:10.1029/91JB00199.

Liu, P., S. Custódio, and R. J. Archuleta (2006), Kinematic inversion of the 2004 M 6.0 Parkfield earthquake including an approximation to site effects, *Bull. Seismol. Soc. Am.*, *96*(4B), S143–S158, doi:10.1785/0120050826.

Lyakhovsky, V., Y. Ben-Zion, and A. Agnon (1997), Distributed damage, faulting, and friction, *J. Geophys. Res.*, *102*(B12), 27,635–27,649.

Marone, S. G., C. H. Scholz, and R. Bilham (1991), On the mechanics of earthquake afterslip, *J. Geophys. Res.*, *96*(B5), 8441–8452, doi:10.1029/91JB00275.

Mendoza, C., and S. H. Hartzell (1988), Aftershock patterns and main shock faulting, *Bull. Seismol. Soc. Am.*, *78*(4), 1438–1449.

Miyazaki, S., P. Segall, J. Fukuda, and T. Kato (2004), Space time distribution of afterslip following the 2003 Tokachi-oki earthquake: Implications for variations in fault zone frictional properties, *Geophys. Res. Lett.*, *31*, L06623, doi:10.1029/2003GL019410.

Monelli, D., and P. M. Mai (2008), Bayesian inference of kinematic earthquake rupture parameters through fitting of strong motion data, *Geophys. J. Int.*, *173*(1), 220–232, doi:10.1111/j.1365-246X.2008.03733.x.

Monelli, D., P. M. Mai, S. Jónsson, and D. Giardini (2009), Bayesian imaging of the 2000 Western Tottori (Japan) earthquake through fitting of strong motion and GPS data, *Geophys. J. Int.*, *176*(1), 135–150, doi:10.1111/j.1365-246X.2008.03943.x.

Montési, L. G. J. (2004), Controls of shear zone rheology and tectonic loading on postseismic creep, *J. Geophys. Res.*, *109*, B10404, doi:10.1029/2003JB002925.

Murray, J., and J. Langbein (2006), Slip on the San Andreas fault at Parkfield, California, over two earthquake cycles, and the implications for seismic hazard, *Bull. Seismol. Soc. Am.*, *96*(4B), S283–S303, doi:10.1785/0120050820.

Okada, Y. (1992), Internal deformation due to shear and tensile faults in a half-space, *Bull. Seismol. Soc. Am.*, *82*, 1018–1040.

Ozawa, S., T. Nishimura, H. Suito, T. Kobayashi, M. Tobita, and T. Imakiire (2011), Coseismic and postseismic slip of the 2011 magnitude-9 Tohoku-Oki earthquake, *Nature*, *475*, 373–376.

Peng, Z., and P. Zhao (2009), Migration of early aftershocks following the 2004 Parkfield earthquake, *Nature*, *2*, 877–881.

Perfettini, H., and J.-P. Avouac (2004), Postseismic relaxation driven by brittle creep: A possible mechanism to reconcile geodetic measurements and the decay rate of aftershocks, application to the Chi-Chi earthquake, Taiwan, *J. Geophys. Res.*, *109*, B02304, doi:10.1029/2003JB002488.

Perfettini, H., and J.-P. Avouac (2007), Modeling afterslip and aftershocks following the 1992 Landers earthquake, *J. Geophys. Res.*, *112*, B07409, doi:10.1029/2006JB004399.

Perfettini, H., J.-P. Avouac, and J.-C. Ruegg (2005), Geodetic displacements and aftershocks following the 2001 Mw = 8.4 Peru earthquake: Implications for the mechanics of the earthquake cycle along subduction zones, *J. Geophys. Res.*, *110*, B09404, doi:10.1029/2004JB003522.

Pollitz, F., P. Banerjee, K. Grijalva, B. Nagarajan, and R. Bürgmann (2008), Effect of 3-D viscoelastic structure on post-seismic relaxation from the 2004 M = 9.2 Sumatra earthquake, *Geophys. J. Int.*, *173*(1), 189–204, doi:10.1111/j.1365-246X.2007.03666.x.

Pritchard, M. E., C. Ji, and M. Simons (2006), Distribution of slip from 11 Mw > 6 earthquakes in the northern Chile subduction zone, *J. Geophys. Res.*, *111*, B10302, doi:10.1029/2005JB004013.

Reuter, M., S. Biasotti, D. Giorgi, G. Patane, and M. Spagnuolo (2009), Discrete Laplace-Beltrami operators for shape analysis and segmentation, *Comput. Graphics*, *33*(3), 381–390, doi:10.1016/j.cag.2009.03.005.

Rolandone, F., D. Dreger, M. Murray, and R. Bürgmann (2006), Coseismic slip distribution of the 2003 Mw 6.6 San Simeon earthquake, California, determined from GPS measurements and seismic waveform data, *Geophys. Res. Lett.*, *33*, L16315, doi:10.1029/2006GL027079.

Ryder, I., B. Parsons, T. J. Wright, and G. J. Funning (2007), Post-seismic motion following the 1997 Manyi (Tibet) earthquake: InSAR observations and modelling, *Geophys. J. Int.*, *169*(3), 1009–1027, doi:10.1111/j.1365-246X.2006.03312.x.

Savage, J. C., M. Lisowski, and J. L. Svarc (1994), Postseismic deformation following the 1989(M = 7.1) Loma Prieta, California, earthquake, *J. Geophys. Res.*, *99*, 13,757–13,765, doi:10.1029/94JB00507.

Savage, J. C., J. L. Svarc, and S. Yu (2005), Postseismic relaxation and transient creep, *J. Geophys. Res.*, *110*, B11402, doi:10.1029/2005JB003687.

Savage, J. C., J. L. Svarc, and S.-B. Yu (2007), Postseismic relaxation and aftershocks, *J. Geophys. Res.*, *112*, B06406, doi:10.1029/2006JB004584.

Scholz, C. H. (1968), Microfractures, aftershocks, and seismicity, *Bull. Seismol. Soc. Am.*, *58*, 1117–1130.

Thurber, C., H. Zhang, F. Waldhauser, J. Hardebeck, A. Michael, and D. Eberhart-Phillips (2006), Three-dimensional compressional wavespeed model, earthquake relocations, and focal mechanisms for the Parkfield, California, region, *Bull. Seismol. Soc. Am.*, *96*(4B), S38–S49, doi:10.1785/0120050825.

Toda, S., R. S. Stein, P. A. Reasenberg, J. H. Dieterich, and A. Yoshida (1998), Stress transferred by the 1995 Mw = 6.9 Kobe, Japan, shock: Effects on aftershocks and future earthquake probabilities, *J. Geophys. Res.*, *103*(B10), 24,543–24,565, doi:10.1029/98JB00765.

Waldhauser, F., W. L. Ellsworth, D. P. Schaff, and A. Cole (2004), Streaks, multiplets, and holes: High-resolution spatio-temporal behavior of Parkfield seismicity, *Geophys. Res. Lett.*, *31*, L18608, doi:10.1029/2004GL020649.

Wang, L., R. Wang, F. Roth, B. Enescu, S. Hainzl, and S. Ergintav (2009), Afterslip and viscoelastic relaxation following the 1999 M7.4 İzmit earthquake, from GPS measurements, *Geophys. J. Int.*, *178*(3), 1220–1237, doi:10.1111/j.1365-246X.2009.04228.x.

Wang, L., S. Hainzl, M. S. Özeren, and Y. Ben-Zion (2010), Postseismic deformation induced by brittle rock damage of aftershocks, *J. Geophys. Res.*, *115*, B10422, doi:10.1029/2010JB007532.

Wells, D. W., and K. J. Coppersmith (1994), New empirical relationships among magnitude, rupture length, rupture width, rupture area, and surface displacement, *Bull. Seismol. Soc. Am.*, *84*(4), 974–1002.

Woessner, J., D. Schorlemmer, S. Wiemer, and P. M. Mai (2006), Spatial correlation of aftershock locations and on-fault main shock properties, *J. Geophys. Res.*, *111*, B08301, doi:10.1029/2005JB003961.

Yabuki, T., and M. Matsu'ura (1992), Geodetic data inversion using a Bayesian information criterion for spatial distribution of fault slip, *Geophys. J. Int.*, *109*, 363–375, doi:10.1111/j.1365-246X.1992.tb00102.x.

Zhao, P., Z. Peng, Z. Shi, M. A. Lewis, and Y. Ben-Zion (2009), Variations of the velocity contrast and rupture properties of M6 earthquakes along the Parkfield setction of the San Andreas fault, *Geophys. J. Int.*, *180*, 765–780.